

# We are IntechOpen, the world's leading publisher of Open Access books Built by scientists, for scientists

6,900

Open access books available

186,000

International authors and editors

200M

Downloads

Our authors are among the

154

Countries delivered to

TOP 1%

most cited scientists

12.2%

Contributors from top 500 universities



WEB OF SCIENCE™

Selection of our books indexed in the Book Citation Index  
in Web of Science™ Core Collection (BKCI)

Interested in publishing with us?  
Contact [book.department@intechopen.com](mailto:book.department@intechopen.com)

Numbers displayed above are based on latest data collected.  
For more information visit [www.intechopen.com](http://www.intechopen.com)



# The Elliptical Elastic-Plastic Microcontact Analysis

Jung Ching Chung  
*Department of Aircraft Engineering,  
Air Force Institute of Technology  
Taiwan ROC*

## 1. Introduction

The elastic-plastic contact of a flat and an asperity which shape is a sphere or an ellipsoid is a fundamental problem in contact mechanics. It is applicable in tribological problems arising from the points of contact between two rough surfaces, such as gear teeth, cam and follower and micro-switches etc. Indeed, numerous works on the contact of rough surfaces were published so far (see review by Liu et al.). Many of these works are based on modeling the contact behavior of a single spherical asperity, which is then incorporated in a statistical model of multiple asperity contact. Based on the Hertz theory, the pioneering work on contact models of pure elastic sphere was developed by Greenwood and Williamson (GW). The GW model used the solution of the frictionless contact of an elastic hemisphere and a rigid flat to model an entire contacting surface of asperities with a postulated Gaussian height distribution. The basic GW model had been extended to include such aspects as curved surfaces (by Greenwood and Tripp), two rough surfaces with misaligned asperities (by Greenwood and Tripp) and non-uniform radii of curvature of asperity peaks (by Hisakado). Abbott and Firestone introduced the basic plastic contact model, which was known as surface micro-geometry model. In this model the contact area of a rough surface is equal to the geometrical intersection of the original undeformed profile with the flat. Based on the experimental results, Pullen and Williamson proposed a volume conservation model for the fully plastic contact of a rough surface.

The works on the above two models are suitable for the pure elastic or pure plastic deformation of contacting spheres. In order to bridge the two extreme models, elastic and fully plastic, Chang et al. (CEB model) extended the GW model by developing an elastic-plastic contact model that incorporated the effect of volume conservation of a sphere tip above the critical interference. Numerical results obtained from the CEB model are compared with the other existing models. In the CEB model, there is no transition regime from the elastic deformation to the fully plastic deformation regime. These deficiencies triggered several modifications by other researchers. Zhao et al. (the ZMC model) used mathematical smoothing expressions to incorporate the transition of the contact load and contact area expression between the elastic and fully plastic deformation regions. Kogut and Etsion (KE model) performed a finite element analysis on the elastic-plastic contact of a deformable sphere and a rigid flat by using constitutive laws appropriate to any mode of deformations. It offered a general dimensionless relation for the contact load, contact area

and mean contact pressure as a function of contact interferences. Jackson and Green had done recently a similar work. In this work, it accounted for geometry and material effects, which were not accounted for in the KE model. Jackson et al. presented a finite element model of the residual stresses and strains that were formed after an elastoplastic hemispherical contact was unloaded. This work also defines an interference at which the maximum residual stress transitions from a location below the contact region and along the axis of symmetry to one near to the surface at the edge of the contact radius (within the pileup).

The aforementioned models deal with rough surfaces with isotropic contacts. However, rough surface may have asperities with various curvatures that the different ellipticity ratios of the micro-contacts formed. Bush et al. treated the stochastic contact summits of rough surfaces to be parabolic ellipsoids and applied the Hertzian solution for their deformations. McCool took account of the interaction between two neighboring asperities and modelled the elastic-plastic contact of isotropic and anisotropic solid bodies. Horng extended the CEB model to consider rough surfaces with elliptic contacts and determined the effects of effective radius ratio on the microcontact behavior. Jeng and Wang extend the Horng's work and the ZMC model to the elliptical contact situation by incorporating the elastic-plastic deformation effect of the anisotropy of the asperities. Chung and Lin used an elastic-plastic fractal model for analyzing the elliptic contact of anisotropic rough surfaces. Buczkowski and Kleiber concentrated their study on building an elasto-plastic statistical model of rough surfaces for which the joint stiffness could be determined in a general way. Lin and Lin used 3-D FEM to investigate the contact behavior of a deformable ellipsoid contacting with a rigid flat in the elastoplastic deformation regime. The above works provided results for the loaded condition case. Calculations of the stress distribution at the points of the compression region only under normal load within the ellipse of contact were dealt with in a number of works. The combined action of normal and tangential loads was also discussed in some works whose authors examined the stress conditions at points of an elastic semi-space. However, the above-mentioned works just discussed the distribution of stresses under the elliptical spot within the elastic deformation regime. The distribution of stresses within the elastoplastic deformation regime was still omitted. Chung presented a finite element model (FEM) of the equivalent von-Mises stress and displacements that were formed for the different ellipticity contact of an ellipsoid with a rigid flat.

## 2. Important

The present chapter is presented to investigate the contact behavior of a deformable ellipsoid contacting a rigid flat in the elastoplastic deformation regime. The material is modeled as elastic perfectly plastic and follows the von-Mises yield criterion. Because of geometrical symmetry, only one-eighth of an ellipsoid is needed in the present work for finite element analysis (FEA). Multi-size elements were adopted in the present FEA to significantly save computational time without losing precision. The inception of the elastoplastic deformation regime of an ellipsoid is determined using the theoretical model developed for the yielding of an elliptical contact area.  $k_e$  is defined as the ellipticity of the ellipsoid before contact, so the contact parameters shown in the elastoplastic deformation regime are evaluated by varying the  $k_e$  value. If the ellipticity ( $k$ ) of an elliptical contact area is defined as the length ratio of the minor-axis to the major-axis, it is asymptotic to the  $k_e$  value when the interference is sufficiently increased, irrespective of the  $k_e$  value. The ellipticity ( $k$ ) of an elliptical contact area varies with

the  $k_e$  parameter. The  $k$  values evaluated at various dimensionless interferences and two  $k_e$  values ( $k_e=1/2$  and  $k_e=1/5$ ) are presented. Both interferences, corresponding to the inceptions of the elastoplastic and fully plastic deformation regimes, are determined as a function of the ellipticity of the ellipsoid ( $k_e$ ).

The work also presents the equivalent von-Mises stress and displacements that are formed for the different ellipticities. According to the results of Johnson, Sackfield and Hills, the severest stress always occurs in the  $z$ -axis. In this work, we can get the following result: the smaller the ellipticity of the ellipsoid is, the larger the depth of the first yield point from the ellipsoid tip happens. The FEM produces contours for the normalized normal and radial displacement as functions of the different interference depths. The evolution of plastic region in the asperity tip for a sphere ( $k_e=1$ ) and an ellipsoid with different ellipticities ( $k_e=1/2$  and  $k_e=1/5$ ) is shown with increasing interferences. It is interesting to note the behavior of the evolution of the plastic region in the ellipsoid tip for different ellipticities,  $k_e$ , is different. The developments of the plastic region on the contact surface are shown in more details. When the dimensionless contact pressure is up to 2.5, the uniform contact pressure distribution is almost prevailing in the entire contact area. It can be observed clearly that the normalized contact pressure ascends slowly from the center to the edge of the contact area for a sphere ( $k_e=1$ ), almost has uniform distribution prevailing the entire contact area for an ellipsoid ( $k_e=1/2$ ), and descends slowly from the center to the edge of the contact area for an ellipsoid ( $k_e=1/5$ ). The differences in the microcontact parameters such as the contact pressure, the contact area, and contact load evaluated at various interferences and two  $k_e$  values are investigated.

The elastic-plastic fractal model of the elliptic asperity for analyzing the contact of rough surfaces is presented. Comparisons between the fractal model and the classical statistical model are discussed in this work. Four plasticity indices ( $\psi = 0.5, 1, 2, \text{ and } 2.5$ ) for the KE (Kogut and Etsion) model are chosen. The topothesy ( $G$ ) and fractal dimension ( $D$ ) values, which are corresponding to these four plasticity indices in the present model, will thus be determined.

### 3. Theoretical background

In the present chapter, Figure 1 shows that a deformable ellipsoid tip contacts with a rigid flat. The lengths of the semi-major axis of an ellipsoid and the semi-minor axis are assumed to be  $cR$  ( $1 \leq c < \infty$ ) and  $R$ , respectively. From the geometrical analysis, the radii of curvature at the tip of an ellipsoid,  $R_{1x}(=c^2R)$  and  $R_{1z}(=R)$ , are obtained. the ellipticity of an ellipsoid is defined as  $k_e$ , and  $k_e = (R_{1z} / R_{1x})^{1/2} = 1 / c = R / cR$ . For  $c = 1$ ,  $k_e = 1$ , corresponds to the spherical contact; for  $c \rightarrow \infty$ ,  $k_e = 0$ , corresponds to the cylindrical contact. The simulations by FEM are carried out under the condition of a given interference  $\delta$  applied to the microcontact formed at the tip of an ellipsoid. Because of geometrical symmetry, only one-eighth of an ellipsoid volume is needed in the finite element analysis (see Figure 2). At an interference,  $\delta$ , an elliptical contact area is formed with a semi-major axis,  $a$ , and a semi-minor axis,  $b$ . The length ratio  $k$  is here defined as  $k=b/a$ , which is called the ellipticity of this elliptical contact area. The material of this ellipsoid is modeled as elastic perfectly plastic with identical behavior in tension and compression.

The contact area of an asperity here is elliptical in shape, having two semi-axis lengths,  $a$  and  $b$  ( $b < a$ ), in the present study. The eccentricity of the contact ellipse ( $e$ ) is

$$e = \left(1 - \frac{b^2}{a^2}\right)^{1/2} \quad (1)$$

Define the  $C'$  parameter as  $C' \equiv (ab)^{1/2}$ , this parameter has been derived by Johnson [25] as

$$C' = (ab)^{1/2} = \left(\frac{3FR_e}{4E^*}\right)^{1/3} \{F_1(e)\}^{1/3} \quad (2)$$

Where  $R_e$  denotes the effective radius of curvature of an asperity.

$$F_1(e) = \frac{4}{\pi e^2} \left(\frac{b}{a}\right)^{3/2} \left\{ \left[ \left(\frac{a}{b}\right)^2 E(e) - K(e) \right] [K(e) - E(e)] \right\}^{1/2} \quad (3)$$

$E^*$  in Eq.(1) denotes the effective Young's modulus of two solid contact bodies with the Young's moduli,  $E_1$  and  $E_2$ , and the Poisson ratios,  $\nu_1$  and  $\nu_2$ , respectively. It is stated as

$$\frac{1}{E^*} = \frac{1 - \nu_1^2}{E_1} + \frac{1 - \nu_2^2}{E_2} \quad (4)$$

Where  $F$  denotes the normal load of an asperity at the Hertz contact area.  $K(e)$  and  $E(e)$  in the formula of  $F_1(e)$  denote the complete first and second elliptic integrals of argument ( $e$ ), respectively. They are expressed by Johnson as

$$K(e) = \int_0^{\pi/2} \frac{d\theta}{\sqrt{1 - e^2 \sin^2 \theta}} \quad (5)$$

$$E(e) = \int_0^{\pi/2} \sqrt{1 - e^2 \sin^2 \theta} \, d\theta \quad (6)$$

The onset of the plastic yield of ductile materials usually occurs when the von Mises' shear strain-energy criterion reaches

$$\mathcal{J}_2^* = (k')^2 = \frac{Y^2}{3} \quad (7)$$

Where  $\mathcal{J}_2^*$  is the maximum value of the second invariant of the deviator stress tensor ( $\mathcal{J}_2$ ) at yielding and  $k'$  is the material yield stress in simple shear. The second invariant of the deviator stress tensor can be written as:

$$\mathcal{J}_2 = \frac{1}{6} \left[ (\sigma_1 - \sigma_2)^2 + (\sigma_2 - \sigma_3)^2 + (\sigma_3 - \sigma_1)^2 \right] \quad (8)$$

Where  $\sigma_1$ ,  $\sigma_2$ , and  $\sigma_3$  are the three principal stresses. In the study of Sackfield and Hills, the stress distributions formed by the Hertz contact pressure acting on an elliptical contact surface were developed and it was shown that the severest stress always occurs on the z axis, and the maximum value of  $J_2$  should occur at a certain point on this axis. The position of the point  $Z^*$  can be determined from the solution of the following equation:

$$\frac{\partial J_2}{\partial Z} \Big|_{z=Z^*} = 0 \quad (9)$$

Where  $Z = z/a$  is the dimensionless z-coordinate, and  $Z^*$  denotes the  $Z$  parameter when  $J_2$  has the maximum value at yielding.

The interference at the initial point of yielding is known as the critical interference,  $\delta_y$ , which is derived analytically by using the von Mises yield criterion and given by Lin and Lin as

$$\delta_y = \left( \frac{9F_y^2}{16E^*R_e} \right)^{\frac{1}{3}} \frac{2}{\pi} k^2 [F_1(e)]^{-\frac{1}{3}} K(e) \quad (10)$$

Where

$$F_y = \frac{\pi^3 R_e^2}{6E^*} [F_1(e)]^2 [K(k, \nu, Z^*) Y]^3 \quad (11)$$

The corresponding critical contact area is expressed as

$$a_c = \pi \left( \frac{3F_y R_e}{4E^*} \right)^{\frac{2}{3}} [F_1(e)]^{\frac{2}{3}} \quad (12)$$

Where  $Y$  is the yielding stress of the ellipsoid material.  $K(k, \nu, Z^*)$  denotes the factor of the maximum contact pressure arising at yielding. This factor is expressed as a function of the ellipticity of the contact area,  $k$ , and the Poisson ratio of a material,  $\nu$ .  $Z^*$  is the location of first yielding point on z-coordinate. The derivation of  $K(k, \nu, Z^*)$  is shown in Lin and Lin's work. Ellipsoid deforms elastically as  $\delta/\delta_y < 1$ . When  $\delta/\delta_y > 1$  the ellipsoid is in the elastoplastic deformation.

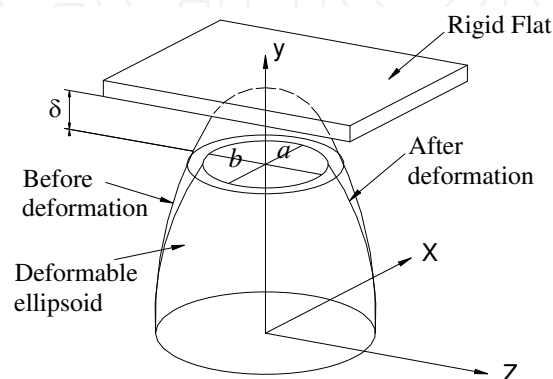


Fig. 1. The contact schematic diagram of a rigid flat with an ellipsoid.

#### 4. Finite element model

In the present work, a commercial ANSYS-8.0 software package is applied to determine the elastoplastic regime arising at a deformable ellipsoid in contact with a rigid flat (see figure 2). There are two ways to simulate the contact problem. The first applies a force to the rigid body and then computes the resulting displacement. The second applies a displacement and then computes the resulting contact force. The present finite element solution is generated under a given interference  $\delta$  applied to the contact area formed at the tip of an ellipsoid. This method is used because the resulting solution converges more rapidly than the former. In order to satisfy the geometrically symmetric condition and to assure that the nodes on the boundary of  $y = 0$  are far away from the contact area, the selection of one-eighth of the ellipsoidal volume as the simulation domain is made. Several option settings of ANSYS-8.0 software package have been made to reduce error in finite element calculations. The option of a static large displacement is adopted for the calculations in the elastoplastic and fully plastic regimes. The choice of the displacement style is based on the stress-strain (or load-displacement) behavior exhibited in each of these two deformation regimes. The ellipsoid is assumed to be an elastic-perfectly plastic material with identical behavior in tension and compression. This assumption was also made in the studies of Kogut and Etsion, and Jackson and Green. Frictionless and standard contact was also assumed as in their numerical simulations.

To increase the accuracy and efficiency of computation, one-eighth of an ellipsoid is used. Several mesh refinements have been performed to reduce the error in calculating von-Mises stress. For this investigation ANSYS element types 10-node, tetrahedron SOLID 92 element is selected for this nonlinear contact problem. Three sizes,  $0.0005R$ ,  $0.0008R$ , and  $0.001R$  ( $R$ : the semi-minor radius of ellipsoid), are the smallest element sides in the contact region set for ellipsoids with  $k_e = 1, 1/2$  and  $1/5$ , respectively. In the present numerical model, the mesh size was refined according to its distance from the  $y$ -axis and the contact area of an ellipsoid. The fine mesh size of the volume element near the tip of the ellipsoid is varied in order to allow the ellipsoid's curvature to be captured and accurately simulated during deformations (see Figure 2). As to the region far away from the  $y$ -axis and the contact area, different coarser element size can be given in order to save computational time without sacrificing the precision of the solutions. As shown in Figure 2, constraints in the  $x$  directions and  $z$  direction are applied to the nodes on the  $x=0$  plane and  $z=0$  plane, respectively, while a constraint in  $y$  direction is applied on the base (the  $y=0$  plane). The boundary condition may be valid for the modeling of asperity contacts for two reasons: (1) the asperities are actually connected to a much larger bulk material at the base and will be significantly restrained there, and (2) since the high stress region occurs near the contact, the boundary condition at the base of the ellipsoid will not greatly effect the solution because of Saint Venant's Principle.

In order to validate the model, mesh convergence must be satisfied. The mesh density is iteratively increased until the contact force and contact area differed by less than 1% between iterations. In the finite element analyses, the resulting meshes consist of at least 124572, 125714, and 222913 elements correspond to ellipsoids with  $k_e = 1, 1/2$  and  $1/5$ , respectively. These three node numbers are sufficient to obtain the numerical solutions with a high precision, compared with the theoretical solutions developed for the elastic deformation region. It is found that an excessive increase in the number of elements does

not bring a significant improvement in the solution precision. The “contact wizard” in the software determines the relationship of the contact pair. The rigid flat is set as “Target”, and the deformable ellipsoid is set as “Contact”.

In addition to mesh convergence, the present work also compares well with the Hertz solution at interference below the critical interference. The numerical solutions for several contact parameters with different  $k_e$  values ( $k_e=1$ ,  $k_e=1/2$  and  $k_e=1/5$ ) are listed in Table 1. The error between the theoretical and numerical solutions for all contact parameters is found to be always less than 1.5%. In the present study, the FKN (contact stiffness) value is varied in a range of 10 to 100 in the finite element analyses. Since precise solutions in all contact parameters are ensured, the accuracy of the solutions in the elastoplastic and fully plastic deformation regimes obtained by the present mesh scheme is ascertainable. Furthermore, because  $k_e = 1$  represents a spherical contact, the present work compares with the results which are obtained by Jackson and Green and shows good agreement.

Since this contact problem is nonlinear and highly difficult to converge. An iterative scheme is used to solve for the solution, the minimum and maximum substeps are set in the range of 10 to 2000 such that  $(\delta / \delta_y) / (\text{substep number})$  has a value varying in the range of 0.05~0.2. This is done to ensure the load increment is sufficiently small at each load step, thus improving the convergence behavior and minimizing the Newton-Raphson equilibrium iterations required.

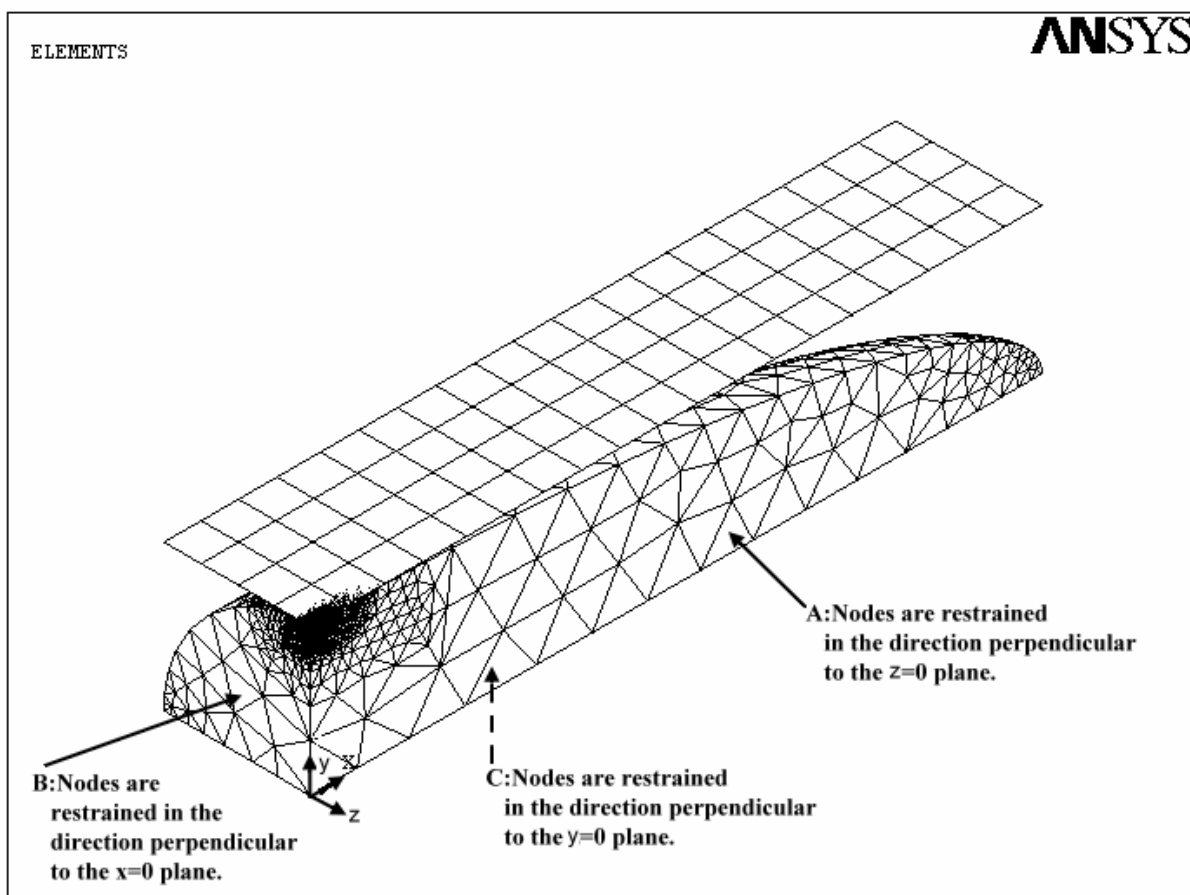


Fig. 2. The finite element analysis and the meshed model for simulations.

	$k_e=1$		$k_e=1/2$		$k_e=1/5$	
	Hertz solution	FEA solution	Hertz solution	FEA solution	Hertz solution	FEA solution
$\delta_y/\delta_{y1}$	1	0.99	1.85	1.83	3.21	3.19
$S_{eqv}/Y$	1	1	1	0.99	1	0.99
$P_{max}/Y$	1.61	1.63	1.65	1.62	1.73	1.74

Table 1. The comparison of numerical evaluated results at the critical interference with the theoretical solutions in the elastic deformation case

## 5. Results and discussion

The results are presented for a range of interferences,  $\delta$ , which are normalized by each corresponding critical interference,  $\delta_y$ , from 1 to 120 for a sphere, 1 to 100 for an ellipsoid ( $k_e=1/2$ ) and 1 to 70 for an ellipsoid ( $k_e=1/5$ ). The factor of the maximum contact pressure arising at yielding criterion,  $K$ , as shown in Eq. 7, is expressed as a function of  $f(k, \nu, Z^*)$ . The used material properties are for a steel material and present as  $\nu=0.3$ ,  $E=2.07 \times 10^{11}$  Pa,  $Y=7 \times 10^8$  Pa, and  $R=10^{-4}$  m. These material properties allow for effective modeling of all the elastoplastic contact regimes in the FEM simulation. The force convergence tolerance is 0.01 for the nonlinear solutions. Once the mesh is generated, computation takes from 1 hour for small interference to 50 hours for large interference by using an IBM p690 computer.

Figure 3-a shows the first yield point in the ellipsoid tip for (a) sphere ( $k_e=1$ ), (b) ellipsoid ( $k_e=1/2$ ), (c) ellipsoid ( $k_e=1/5$ ) while the deformation equals to each critical interference  $\delta_y$ . It is found that the first yield point happens in the larger depth from the ellipsoid tip for the smaller ellipticity of an ellipsoid, where the depth of the first yielding point is calculated as the distance between the top of the tip of an ellipsoid and the locations of the first yielding point. The smaller the ellipticity of the ellipsoid is, the larger the depth from the ellipsoid tip happens. While the first yielding depth values are normalized by the depth of ellipticity  $k_e=1$ , the values corresponding to  $k_e=1$ ,  $k_e=1/2$ ,  $k_e=1/5$  are 1, 1.5 and 1.8, respectively.

Figure 3-b shows the comparisons of the critical interference  $\delta_y$  and the location of the first yielding point with the ellipticity of a contact area  $k$ . The critical interference,  $\delta_y$ , is significantly increased when the ellipticity of a contact area,  $k$ , is reduced. The depth of the first yielding point is deeper as the ellipticity of a contact area becomes smaller. The ellipticity of a contact area,  $k$ , is actually governed by the ellipticity of the ellipsoid. The ellipticities of a contact area formed at the yielding point for  $k_e=1$ ,  $k_e=1/2$ ,  $k_e=1/5$  are  $k=1$ ,  $1/2.5$  and  $1/7.95$  respectively. If the ellipticity of a contact area is smaller, it will correspond to the smaller ellipticity of an ellipsoid. The described phenomena can be seen on figure 3-a.

Figure 4 presents the evolution of the plastic region inside the ellipsoid tip for (a) sphere ( $k_e=1$ ), (b) ellipsoid ( $k_e=1/2$ ) and (c) ellipsoid ( $k_e=1/5$ ) while  $1 \leq \delta/\delta_y \leq 30$ . Connecting the nodes with the equivalent von-Mises stress equals yield stress,  $Y$ , which is recorded by the commercial finite element program ANSYS 8.0, draws the elastic-plastic boundary line.

The behavior of the evolution of the plastic region in the ellipsoid tip for different ellipticities of an ellipsoid,  $k_e$ , is different. The development of plastic region on the contact surface is shown in more details in figure 7.

The evolution of the plastic region inside the ellipsoid tip at larger normalized interference,  $40 \leq \delta / \delta_y \leq 120$ , is shown in figure 5. As the interference increases above  $\delta / \delta_y = 80$ , the normal penetration of the plastic region is coincided at about  $0.805 \times 10^{-4} \text{m}$  as shown in figure 5(a) for a sphere tip ( $k_e = 1$ ). The above phenomena doesn't happen in the ellipsoid tip for ellipticity  $k_e = 1/2$  and  $k_e = 1/5$  at larger interference. The shapes of the plastic region in the ellipsoid tip for different ellipticities are also different.

Figure. 6 presents the three dimension contour plots of the equivalent von-Mises stress on the contact surface for (a) sphere ( $k_e = 1$ ), (b) ellipsoid ( $k_e = 1/2$ ) and (c) ellipsoid ( $k_e = 1/5$ ) at interference  $\delta / \delta_y = 10$ . At this interference the plastic region reaches the contact surface for both a sphere and an ellipsoid, which is shown in more details in figure 7. At this point an elastic core remains locked between the plastic region and the surface for a sphere ( $k_e = 1$ ) and an ellipsoid ( $k_e = 1/2$ ). It is interesting to note that the center of contact surface for an ellipsoid ( $k_e = 1/5$ ) has reached the plastic deformation. The plastic region reaches on both of the center area and an elliptical annular area on the contact surface for an ellipsoid ( $k_e = 1/5$ ). The evolution of the plastic region on the contact surface will behave in a different way for a sphere and both for an ellipsoid tip. At  $\delta / \delta_y = 10$ , the boundary of the plastic region that reaches the contact surface, which is obtained from curve fitting of the finite element analysis numerical results is plotted as figure 7. The lengths of semi-minor contact axis that are normalized by the critical contact radius of a sphere are about 2.4, 3.2 and 4.4 for the sphere ( $k_e = 1$ ), ellipsoid ( $k_e = 1/2$ ) and ellipsoid ( $k_e = 1/5$ ), respectively. The lengths of semi-major contact axis that are normalized by the critical contact radius of a sphere are about 2.4, 6.8 and 23.5 for the sphere ( $k_e = 1$ ), ellipsoid ( $k_e = 1/2$ ) and ellipsoid ( $k_e = 1/5$ ), respectively. The curve fitting length on semi-minor contact axis compared to the curve fitting length on semi-major contact axis is 1/2.13 and 1/5.34 for the ellipsoid ( $k_e = 1/2$ ) and ellipsoid ( $k_e = 1/5$ ), respectively. The above comparison values for the ellipsoid ( $k_e = 1/2$ ) and ellipsoid ( $k_e = 1/5$ ) aren't equal to the ellipticity of an ellipsoid.

Figure 8 presents the evolution of the plastic region on the contact surface for a sphere ( $k_e = 1$ ) while  $10 \leq \delta / \delta_y \leq 120$ . The boundary of the plastic region on the contact surface obtained from curve fitting of the finite element analysis numerical results of nodes is plotted as figure 8. At about  $\delta / \delta_y = 6$  an annular plastic region first reaches the contact surface of a sphere. It is clear to see that an elastic core is locked by the annular plastic region. As the interference increases, the elastic core gradually shrinks and the annular plastic region will increase both to the center and outer line of the contact area. Finally, the elastic core disappears and the plastic region will dominate the most part of the contact area except for the outer annular area surrounded by the elastic region as shown in figure 8. The same conclusions have been obtained in the Kogut and Etsion's studies and are also seen by Jackson and Green.

Figure 9 presents the evolution of the plastic region on the contact surface of an ellipsoid ( $k_e = 1/2$ ) for increasing interference values up to  $\delta / \delta_y = 90$ . Up to  $\delta / \delta_y = 10$  the elastic region dominate the contact surface. At  $\delta / \delta_y = 10$  the plastic region first reaches the contact surface and forms an annular plastic region as shown in Figure 6 and figure 9. For  $10 \leq \delta / \delta_y \leq 30$ , the annular plastic region disappears dramatically and an elliptical plastic

region appears on the center of contact surface. As the interference increases thereafter, the plastic region expands from center toward the edge of the contact surface. Even at this interference  $\delta / \delta_y = 90$ , the plastic region still doesn't coincide with the boundary edge of the contact area. But as figure 15(b) shows, the P/Y value is asymptotic to a constant value at this interference  $\delta / \delta_y = 100$ . Obviously, the interference  $\delta / \delta_y = 90$  is near the inception of the fully plastic deformation for  $k_e = 1/2$ .

Figure 10 presents the evolution of the plastic region on the contact surface of an ellipsoid ( $k_e = 1/5$ ) for increasing interference values up to  $\delta / \delta_y = 70$ . Up to  $\delta / \delta_y = 10$  the elastic region dominates the contact surface. At  $\delta / \delta_y = 10$  the plastic region first reaches the contact surface and forms an annular plastic region as shown in figure 6 and figure 10. In addition to the annular plastic region, the center of the contact surface also forms a plastic subregion. For  $10 \leq \delta / \delta_y \leq 30$  the annular plastic region disappears dramatically and an elliptical plastic region on the center of contact surface extends the original dominated area. As the interference increases thereafter, the plastic region expands from center toward the edge of the contact surface. Even at interference  $\delta / \delta_y = 70$ , the plastic region still doesn't coincide with the boundary edge of the contact area. It can be seen the plastic region extends toward the direction of the major contact axis as the interference increases. But as figure 15(c) shows, the P/Y value is asymptotic to a constant value at this interference  $\delta / \delta_y = 70$ . Obviously, the interference  $\delta / \delta_y = 70$  is near the inception of the fully plastic deformation for  $k_e = 1/5$ .

The normal and radial surface displacements of the nodes on the ellipsoid surface are monitored in order to investigate the deformation of an ellipsoid. As shown in figure 11~14 the normal and radial directions (including semi-major and semi-minor contact axis) correspond to the y- and x-, z-axis, respectively. figure 11 and 12 show the surface displacement,  $U_y / \delta_{y1}$ , in the normal direction for the sphere ( $k_e = 1$ ), ellipsoid ( $k_e = 1/2$ ) and ellipsoid ( $k_e = 1/5$ ) vs. the normalized semi-major axis and semi-minor axis. These plots show the evolution of the surface normal deformation with increasing normalized interferences,  $\delta / \delta_y$ . As expected, the normal deformation on contact surface increases with increasing the normalized interference depth. The boundary between the contact region and the free surface boundary of the ellipsoid can be seen on the line edge in the plots. The slope of the normal displacement on the semi-minor axis is larger than the slope on the semi-major axis. As figure 11 and 12 show, both of the slopes of the normal displacement on the major and minor axis directions for different ellipticities satisfy:  $(k_e = 1) > (k_e = 1/2) > (k_e = 1/5)$ . The slope near the center and edge of contact surface becomes flat. Figure 13 and 14 show the surface displacement,  $U_x / \delta_{y1}$ , in the x radial direction vs. the normalized semi-major axis and the surface displacement,  $U_z / \delta_{y1}$  vs. the semi-minor axis for the sphere ( $k_e = 1$ ), ellipsoid ( $k_e = 1/2$ ) and ellipsoid ( $k_e = 1/5$ ). In the smaller interference depths, the surface displaces radially in mostly the negative direction for a sphere and an ellipsoid. The ellipsoid has the same compression behavior like a sphere. In other word, their contact areas are smaller than the geometrical intersection of the original undeformed profile with the flat in the smaller interference depths. This is because at the smaller normalized interferences, most of the materials in the sphere and ellipsoid are deforming elastically and are allowed to compress. As the interference is larger and significantly increases past the critical deformation, the material of the contact region displaces outward into the positive x

direction and negative  $z$  direction. It can be seen in figure 14 that the radial displacement isn't positive until the normalized interference,  $\delta / \delta_y = 90$ , for a sphere,  $\delta / \delta_y = 50$  for an ellipsoid ( $k_e=1/2$ ) and past  $\delta / \delta_y = 50$  for an ellipsoid ( $k_e=1/5$ ). This bulginess occurs because the yielding material flows plastically and abides by the outlying material of the contact area. As shown in figure 14, the normalized radial displacement,  $U_x / \delta_{y1}$ , become flat near the edge of the semi-major axis of contact area for an ellipsoid ( $k_e=1/5$ ). When compared the boundary of plastic contact area in figure 10, their locations of semi-major contact axis are the same.

Figure 15 presents the normalized contact pressure,  $P/Y$ , profile vs the normalized semi-major contact axis,  $a/a_{c1}$ , and semi-minor contact axis,  $b/a_{c1}$ , for (a) sphere ( $k_e=1$ ) at  $\delta / \delta_y = 120$  (b) ellipsoid ( $k_e=1/2$ ) at  $\delta / \delta_y = 100$ , (c) ellipsoid ( $k_e=1/5$ ) at  $\delta / \delta_y = 70$ . When the normalized interferences,  $\delta / \delta_y$ , equal to 120, 100 and 70, for (a) sphere ( $k_e=1$ ), (b) ellipsoid ( $k_e=1/2$ ) and ellipsoid ( $k_e=1/5$ ), respectively, the uniform contact pressure distribution is almost prevailing in the entire contact area, in which the dimensionless contact pressure is up to 2.5. The determination of the inception of the fully plastic deformation regime is based on the observed phenomenon that the normalized contact pressure and the normalized equivalent von-Mises stresses formed at the contact area have a uniform distribution. If interference is increased further, these uniform normalized contact pressures are found to be unchanged. It can be observed clearly that the normalized contact pressure ascends slowly from the center to the edge of the contact area for a sphere ( $k_e=1$ ), the normalized contact pressure almost has a uniform distribution prevailing the entire contact area for an ellipsoid ( $k_e=1/2$ ), and the normalized contact pressure descends slowly from the center to the edge of the contact area for an ellipsoid ( $k_e=1/5$ ).

Figure 16 shows the variations of the contact-area ellipticity ( $k$ ) in the elastoplastic deformation regime with the ellipticity of ellipsoid ( $k_e$ ) and the dimensionless interference,  $\delta / \delta_y$ . The radii of curvature at the tip of the ellipsoid,  $R_{1x}$  and  $R_{1y}$ , are varied with the contact deformation. The effect of changing the radii of curvature due to contact deformations has been included in the evaluation of the  $k$  value. Data marked by the " $\Delta$ " and " $\square$ " symbols is obtained by assuming  $k_e = 1/2$  and  $k_e = 1/5$ , respectively.

Both data sets show that the ellipticity of contact area,  $k$ , is increased by increasing the dimensionless interference ( $\delta / \delta_y$ ). The data is asymptotic to a constant value equal to the  $k_e$  value associated with it if  $\delta / \delta_y$  is sufficiently large. It should be mentioned that the ellipticity of the contact area in the elastic deformation regime is always a constant value, which is equal to the datum shown in Fig. 16 at  $\delta / \delta_y = 1$ . Therefore, the  $k$  value of an elliptical contact area is a variable when operating in the elastoplastic deformation regime.

The dimensionless contact areas ( $A^*$ ) in the elastoplastic deformation regime varying with the dimensionless interference ( $\delta / \delta_{sy}$ ) and the ellipticity of the ellipsoid ( $k_e$ ) are shown in figure 17. The data for each  $k_e$  value can be expressed in a linear form in the  $\log A^* - \log (\delta / \delta_{sy})$  plot. With the same dimensionless interference  $\delta / \delta_{sy}$ , the dimensionless contact area ( $A^*$ ) is lowered by decreasing the ellipticity of the ellipsoid ( $k_e$ ).

Figure 18 shows for the dimensionless contact load ( $F^*$ ) results needed in the applications of different interferences ( $\delta / \delta_{sy}$ ) and ellipticity values of an ellipsoid ( $k_e$ ). Each of these curves shows a nonlinear relationship between  $F^*$  and  $\delta / \delta_{sy}$ . However, the effect of  $k_e$  on  $F^*$  is exactly opposite to that shown in the dimensionless contact area.

Kogut and Etsion used the plasticity index  $\psi = (\delta_y/\sigma_s)^{-1/2}$  in the evaluations of the deformations arising at the contacts of rough surfaces, where  $\sigma_s$  denotes standard deviation of asperity heights. However, this plasticity index doesn't appear in the fractal analyses. In the Chung and Lin's study, four plasticity indices ( $\psi = 0.5, 1, 2,$  and  $2.5$ ) for the KE model are chosen. The dimensionless topography,  $\bar{G}$ , and fractal dimension,  $D$ , values applied are thus needed to determine on the base of these four plasticity indices. The plasticity index introduced by Greenwood and Williamson can be further expressed as  $\psi = (\delta_y/\sigma_s)^{-1/2} = (\delta_y/\sigma)^{-1/2} (\sigma/\sigma_s)^{-1/2}$ . In the study of Chung and Lin,  $(\delta_y/\sigma)^{-1/2}$  is given as  $\left(\frac{\delta_y}{\sigma}\right)^{-1/2} = \left(\frac{E^*}{KH}\right) \sqrt{\frac{\sigma}{R_e(a_c)}} \left(\frac{\pi}{2} Q(\gamma)\right)^{-1/2} = \left(\frac{E^*}{KH}\right) \sqrt{\frac{1}{R_e(a_c)}} \left(\frac{\pi}{2} Q(\gamma)\right)^{-1/2}$ . In the study of McCool, the relationship between  $\sigma$  and  $\sigma_s$  is given as:  $\left(\frac{\sigma_s}{\sigma}\right)^2 = 1 - \frac{3.717 \times 10^{-4}}{(\eta R \sigma)^2}$ , where the  $\eta R \sigma$  values corresponding to  $\psi = 0.5, 1, 2,$  and  $2.5$  are 0.0302, 0.0414, 0.0541, and 0.0601, respectively. Therefore,  $\left(\frac{\sigma_s}{\sigma}\right)_{\psi=0.5} = 0.7697$ ,  $\left(\frac{\sigma_s}{\sigma}\right)_{\psi=1} = 0.8849$ ,  $\left(\frac{\sigma_s}{\sigma}\right)_{\psi=2.0} = 0.9343$ ,  $\left(\frac{\sigma_s}{\sigma}\right)_{\psi=2.5} = 0.9472$ . By the expression  $\psi = (\delta_y/\sigma)^{-1/2} (\sigma/\sigma_s)^{-1/2}$ , the  $(\delta_y/\sigma)^{-1/2}$  values corresponding to  $\psi = 0.5, 1, 2,$  and  $2.5$  are, 0.5699, 1.063, 2.069 and 2.5687, respectively. The  $\bar{G}$  and  $D$  values corresponding to these four  $\psi$  values are thus shown in figure 19. In figure 19, the ellipticity  $k=1$ . The results of the dimensionless contact load predicted by the Chung and Lin's model are quite close to those predicted by the KE model, irrespective of the plasticity index values.

## 6. Conclusions

The work presents a finite element model (FEM) of the equivalent von-Mises stress and displacements that are formed for an elastoplastic ellipsoid is loaded. The material is modeled as elastic perfectly plastic and follows the von-Mises yield criterion. One-eighth of an ellipsoid in contact with a rigid flat is used to calculate the von-Mises stresses and deformations. A three-dimensional, 10-node, tetrahedron SOLID 92 element was selected for the nonlinear contact problem. Three sizes,  $0.0005R$ ,  $0.0008R$ , and  $0.001R$  ( $R$ : the semi-minor radius of ellipsoid), are the smallest element sides in the contact region set for a sphere with  $k_e=1$  and ellipsoids with  $k_e=1/2$  and  $1/5$ , respectively. The FEM produce the evolution contour plots of the von-Mises stress with the different interferences. It is found that the first yield point happens in the larger depth from the ellipsoid tip for the smaller ellipticity of an ellipsoid. The smaller the ellipticity of the ellipsoid is, the larger the depth from the ellipsoid tip happens. While the first yielding depth values are normalized by the depth of an ellipticity  $k_e=1$ , the values corresponding to  $k_e=1, k_e=1/2, k_e=1/5$  are 1, 1.5 and 1.8, respectively.

At a normalized interference,  $\delta / \delta_y = 10$ , the plastic region reaches the contact surface for a sphere and an ellipsoid, which is shown in more details in figure 7. At this point an elastic core remains locked between the plastic region and the surface for a sphere ( $k_e = 1$ ) and an ellipsoid ( $k_e = 1/2$ ). It is interesting to note that the center of contact surface for an ellipsoid ( $k_e = 1/5$ ) has reached the plastic deformation. The plastic region reaches on both of the center area and an elliptical annular area on the contact surface for an ellipsoid ( $k_e = 1/5$ ).

The normal deformation on the contact surface increases with increasing the normalized interference depth. The boundary between the contact region and the free surface boundary of an ellipsoid can be seen on the line edge in the plots. The slope of normal displacement on the semi-minor axis is larger than the slope on the semi-major axis.

The surface displaces radially in mostly the negative direction for a sphere and an ellipsoid. The ellipsoid has the same compression behavior like a sphere. In other word, their contact areas will shrink compared to the original cutting areas without deformation in the smaller interference depths. As the interference is larger and significantly increases past the critical deformation, the material in contact region displaces outward into the positive x direction and negative z direction.

When the normalized interferences,  $\delta / \delta_y$ , equal to 120, 100 and 70, for (a) sphere ( $k_e = 1$ ), (b) ellipsoid ( $k_e = 1/2$ ) and ellipsoid ( $k_e = 1/5$ ), respectively, the uniform contact pressure distribution is almost prevailing in the entire contact area, in which the dimensionless contact pressure is up to 2.5. It can be observed clearly that the normalized contact pressure ascends slowly from the center to the edge of the contact area for a sphere ( $k_e = 1$ ), the normalized contact pressure almost has a uniform distribution prevailing the entire contact area for an ellipsoid ( $k_e = 1/2$ ), and the normalized contact pressure descends slowly from the center to the edge of the contact area for an ellipsoid ( $k_e = 1/5$ ).

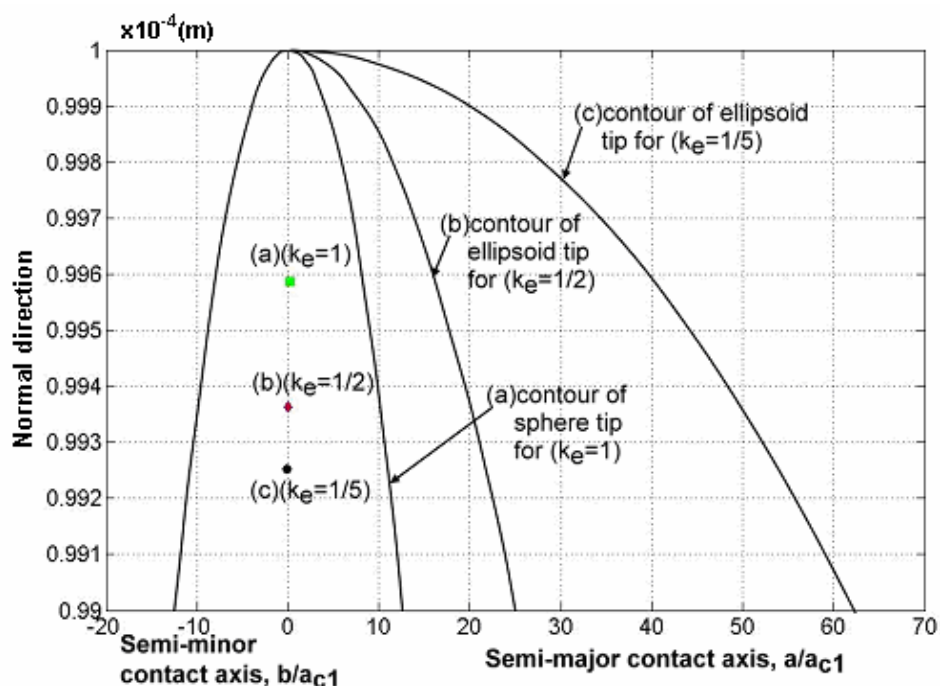
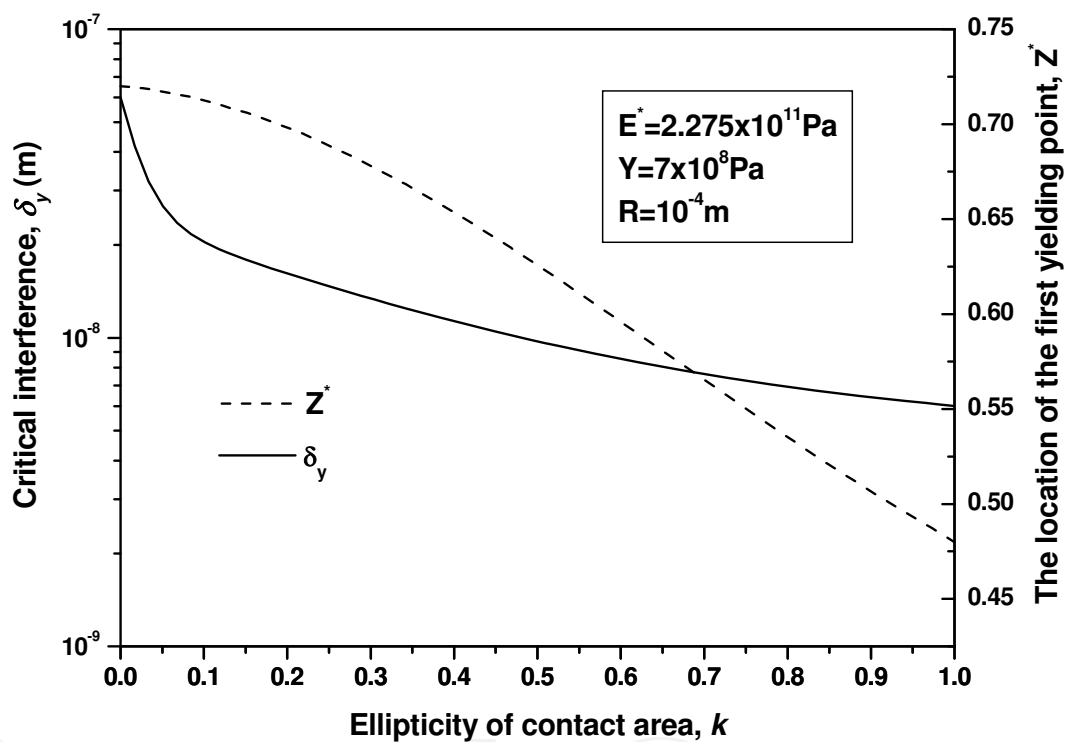


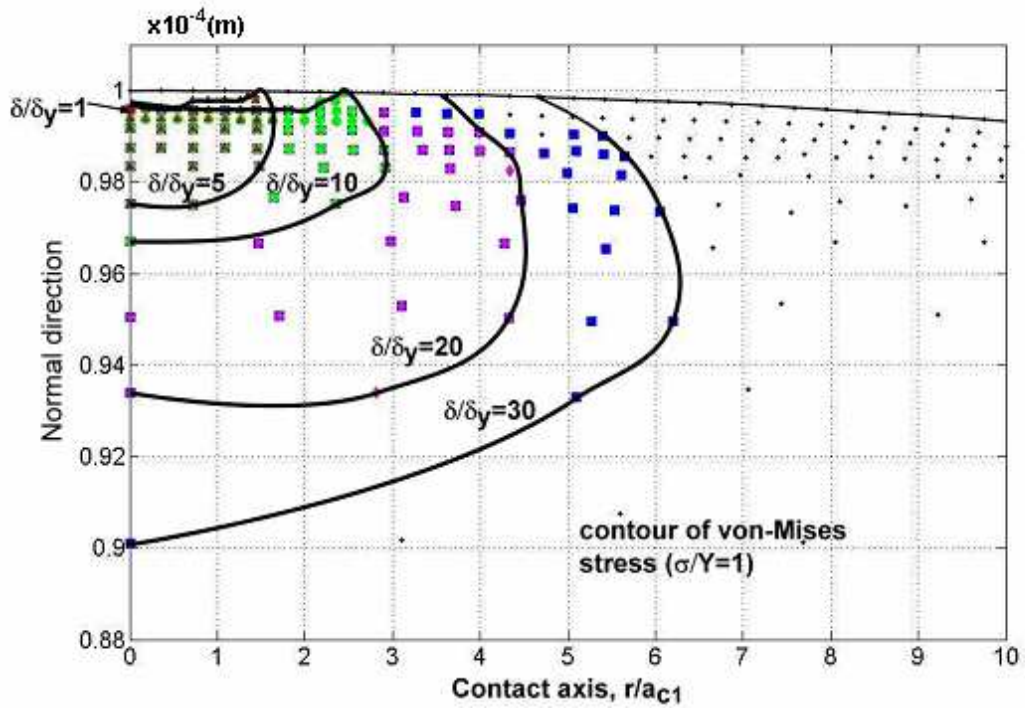
Fig. 3-a. The first yielding point happens in the ellipsoid for (a) sphere ( $k_e = 1$ ) (b) ellipsoid ( $k_e = 1/2$ ) (c) ellipsoid ( $k_e = 1/5$ )

IntechOpen

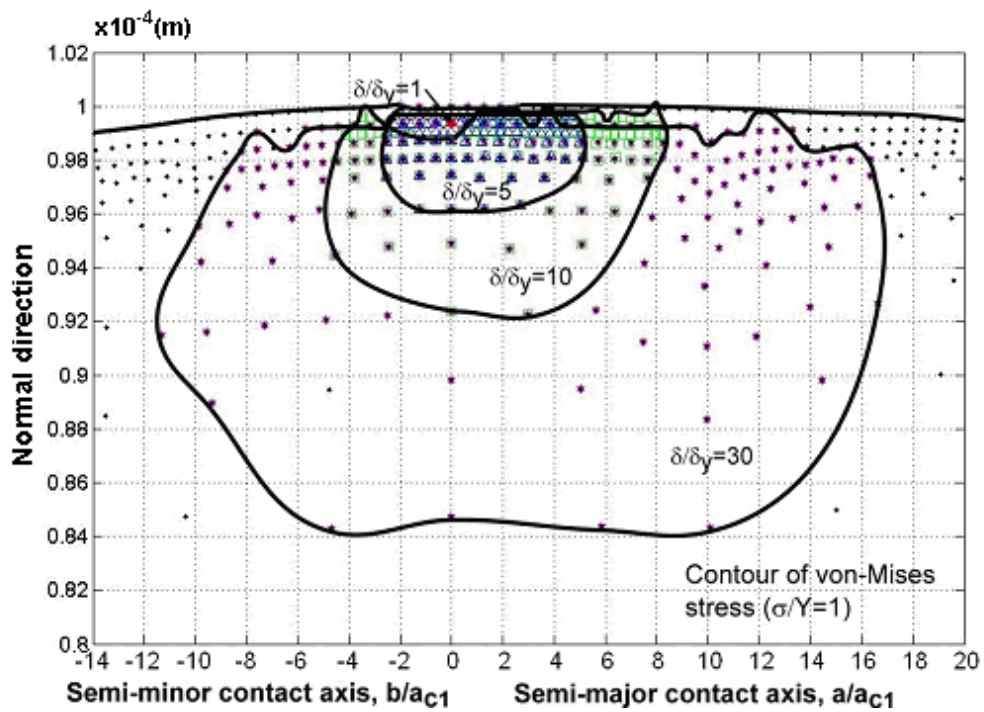


IntechOpen

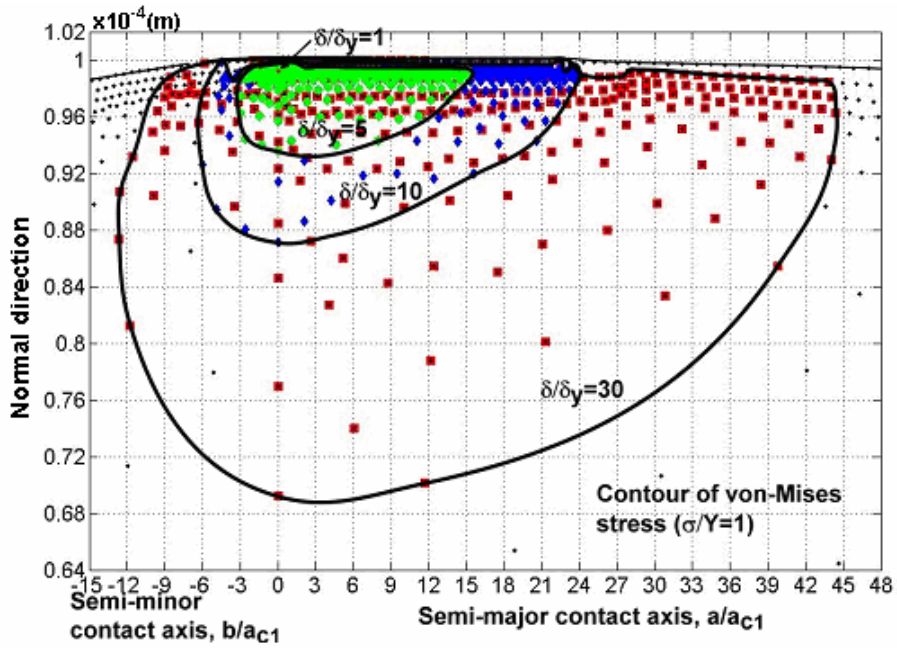
Fig. 3-b. Comparisons of the critical interference and the location of the first yielding point with the ellipticity of a contact area,  $k$



(a)

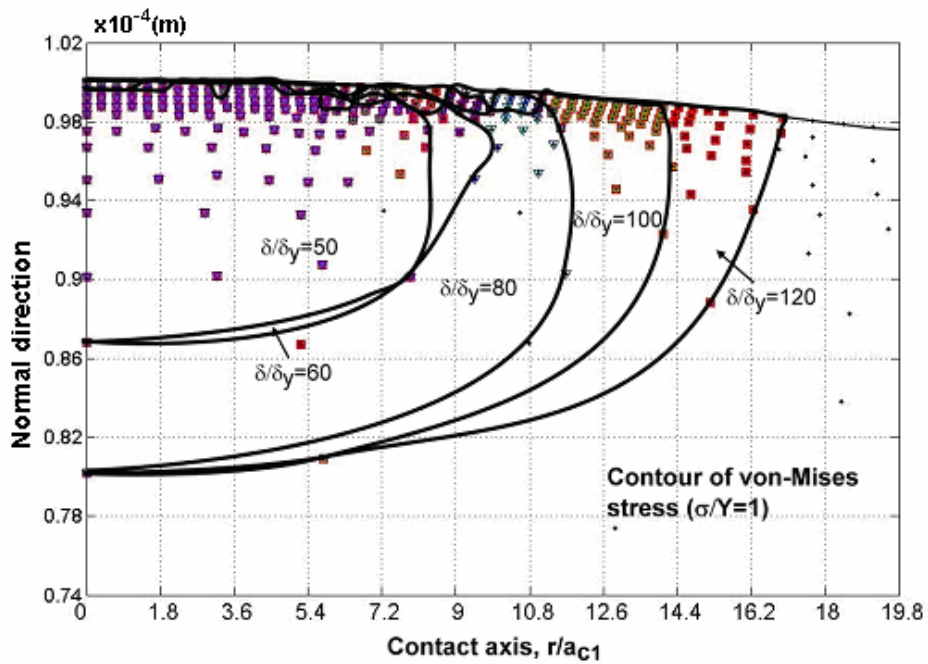


(b)

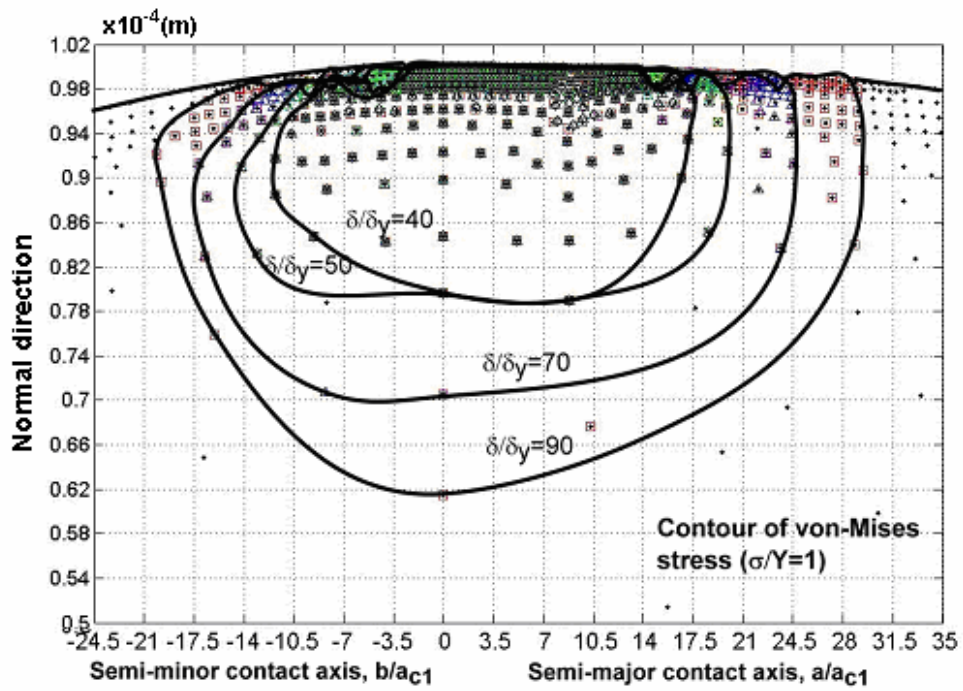


(c)

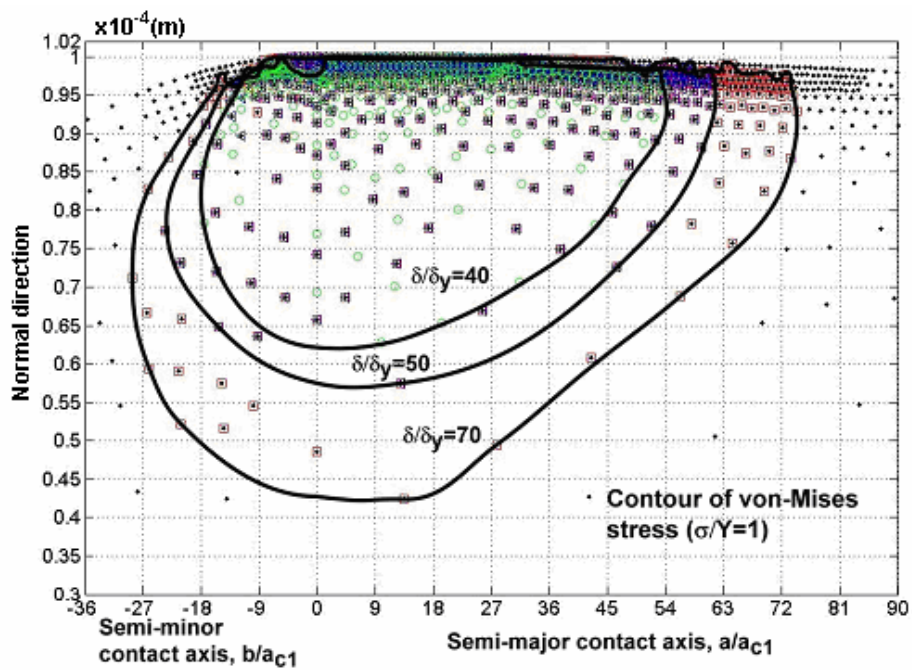
Fig. 4. Evolution of the plastic region in the ellipsoid tip for (a) sphere ( $k_e = 1$ ), (b) ellipsoid ( $k_e = 1/2$ ) and (c) ellipsoid ( $k_e = 1/5$ ) while  $1 \leq \delta / \delta_y \leq 30$



(a)

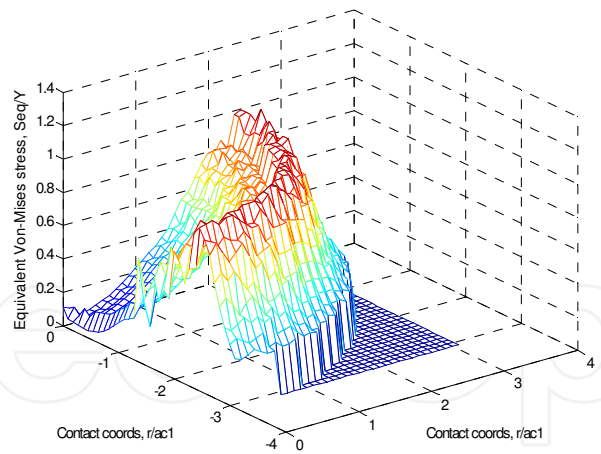


(b)

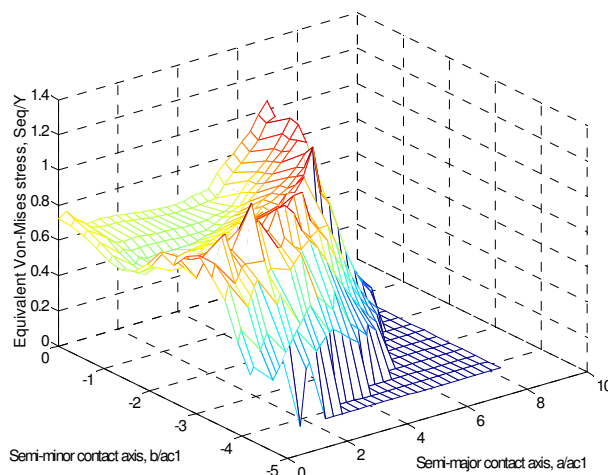


(c)

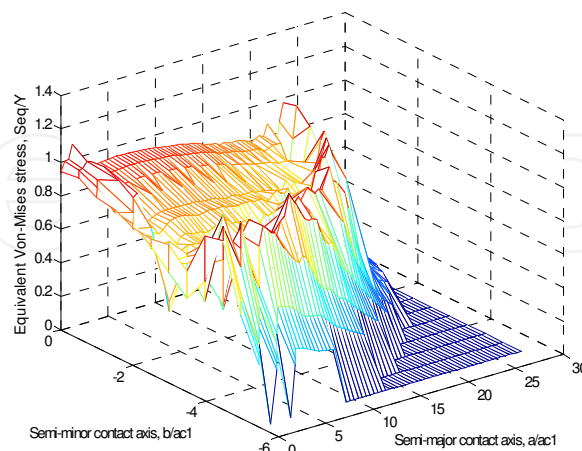
Fig. 5. Evolution of the plastic region in the ellipsoid tip for (a) sphere ( $k_e = 1$ ), (b) ellipsoid ( $k_e = 1/2$ ) and (c) ellipsoid ( $k_e = 1/5$ ) while  $40 \leq \delta / \delta_y \leq 120$



(a)



(b)



(c)

Fig. 6. The equivalent von-Mises stress of contact surface, the plastic region first reaches the contact surface, for (a)sphere ( $k_e = 1$ ) (b)ellipsoid ( $k_e = 1/2$ ) (c)ellipsoid ( $k_e = 1/5$ ) at interference  $\delta / \delta_y = 10$

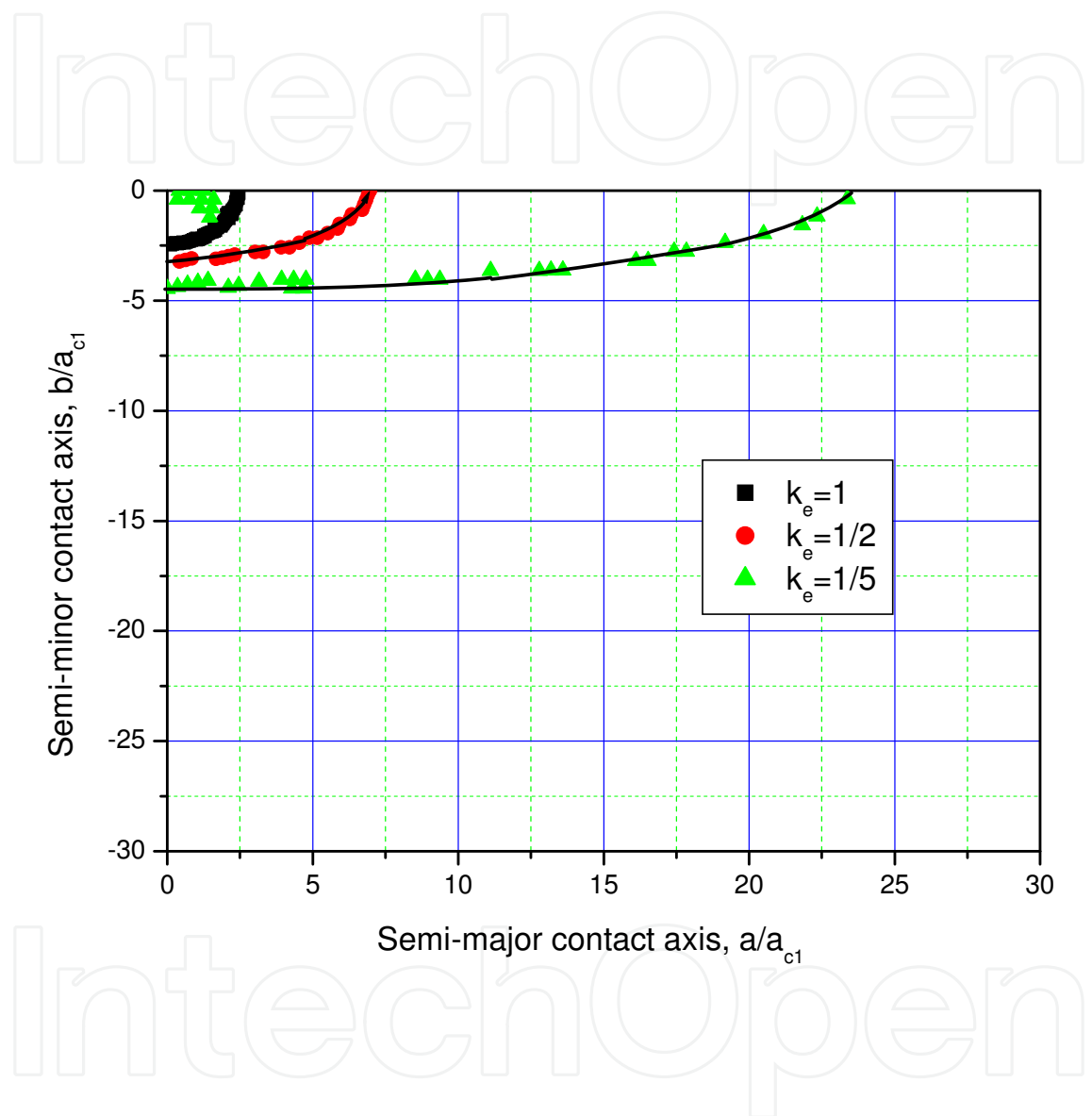
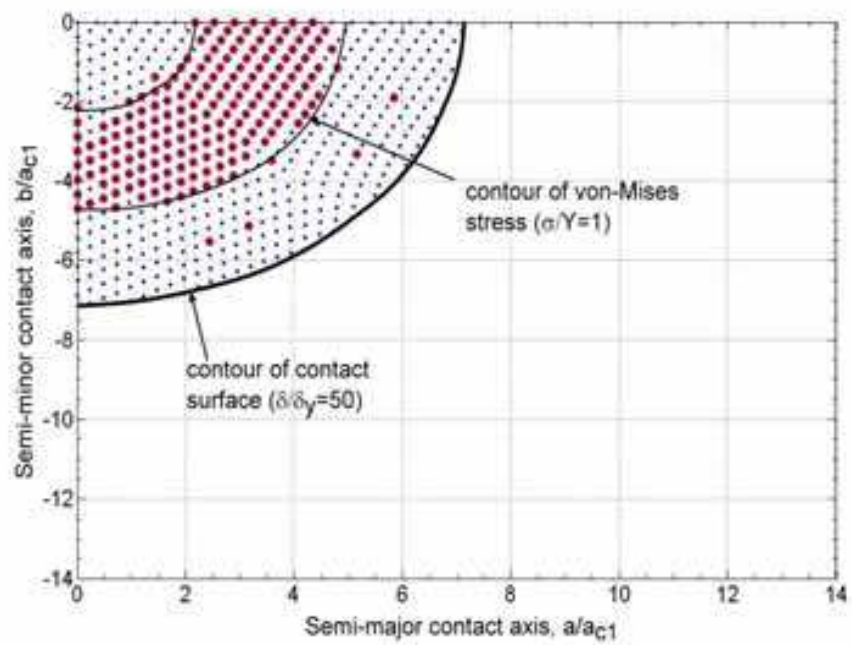
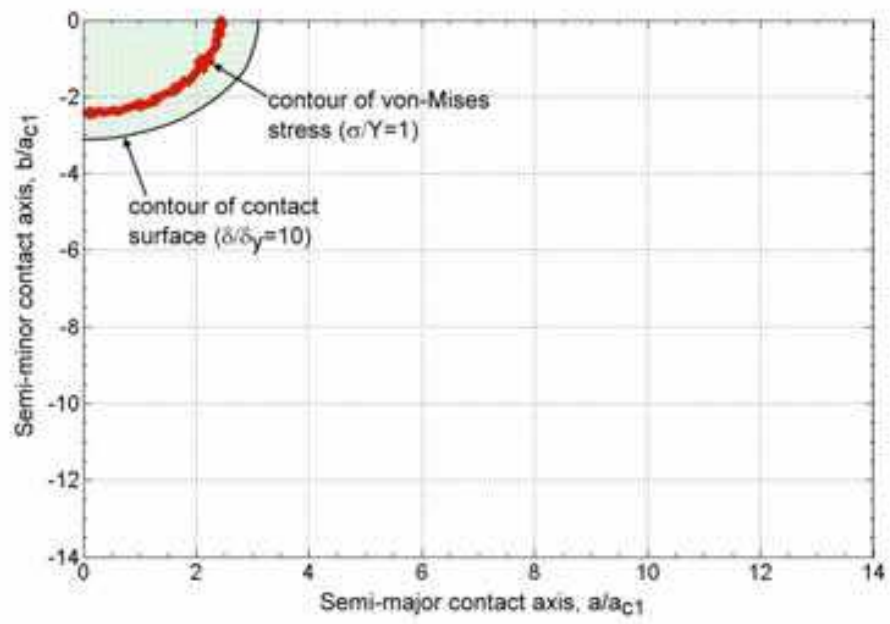


Fig. 7. The Semi-major and minor contact axis of contact surface, the plastic region reaches the contact surface at  $\delta / \delta_y = 10$  for sphere ( $k_e = 1$ ), ellipsoid ( $k_e = 1/2$ ), ellipsoid ( $k_e = 1/5$ ).



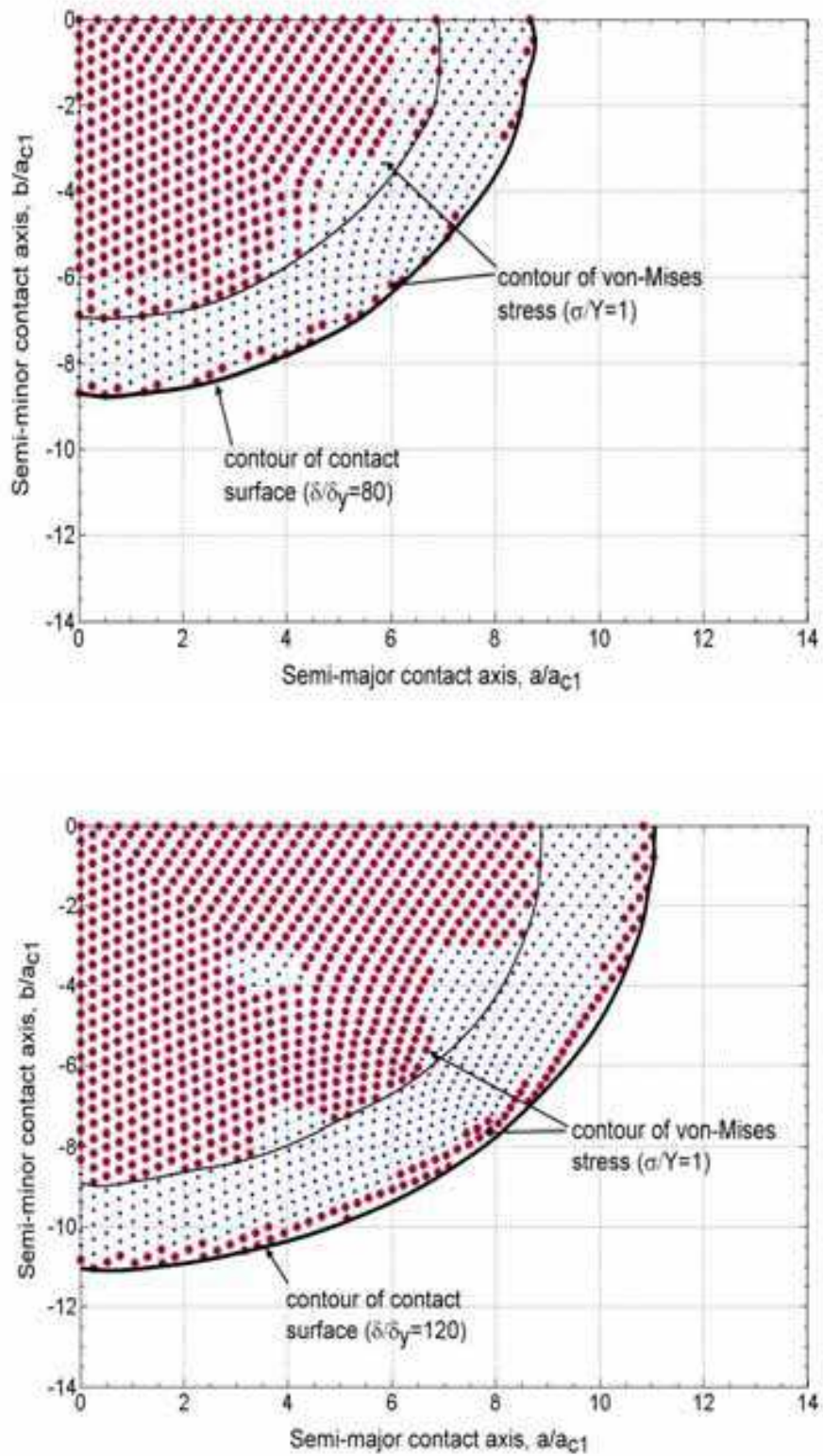
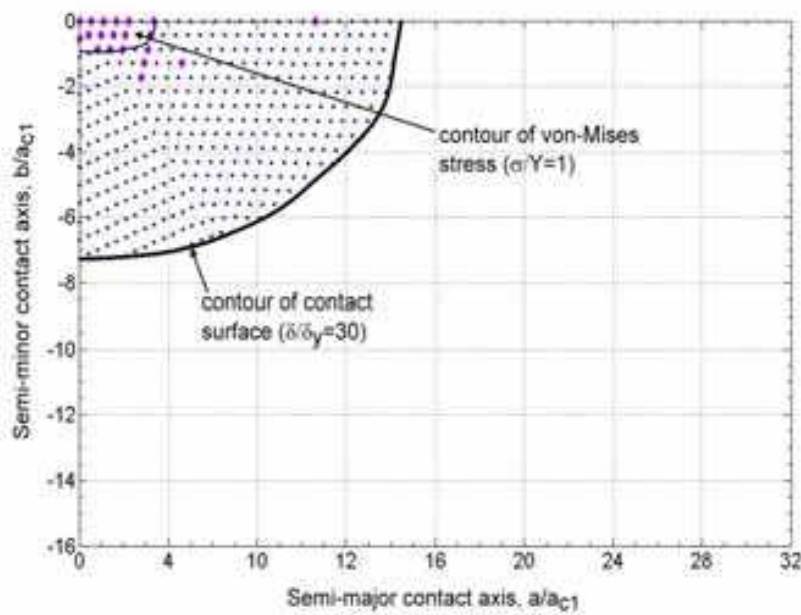
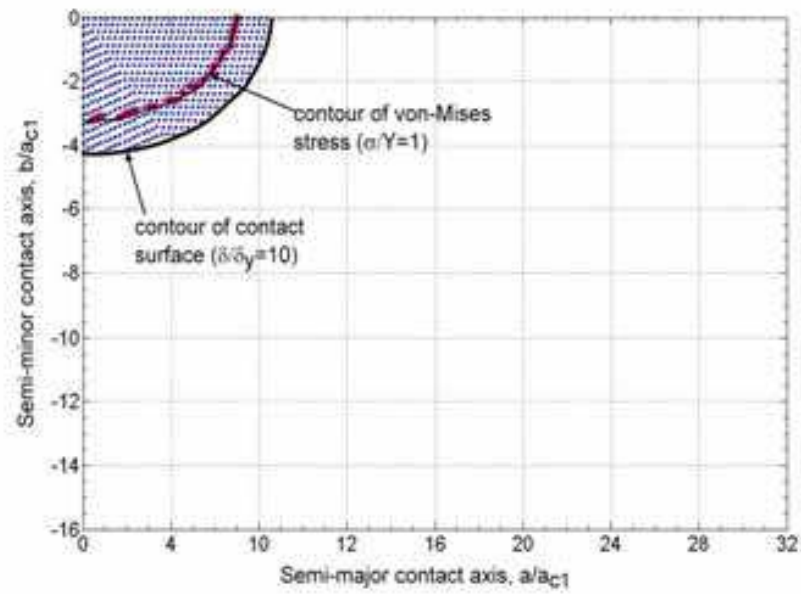


Fig. 8. Evolution of the plastic region on the contact surface for sphere ( $k_e=1$ ) while  $10 \leq \delta / \delta_y \leq 120$



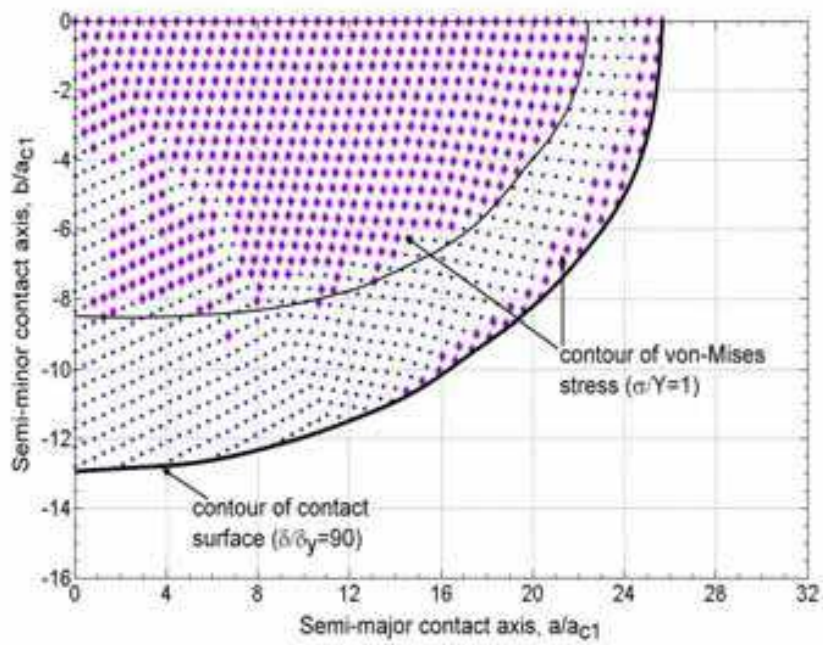
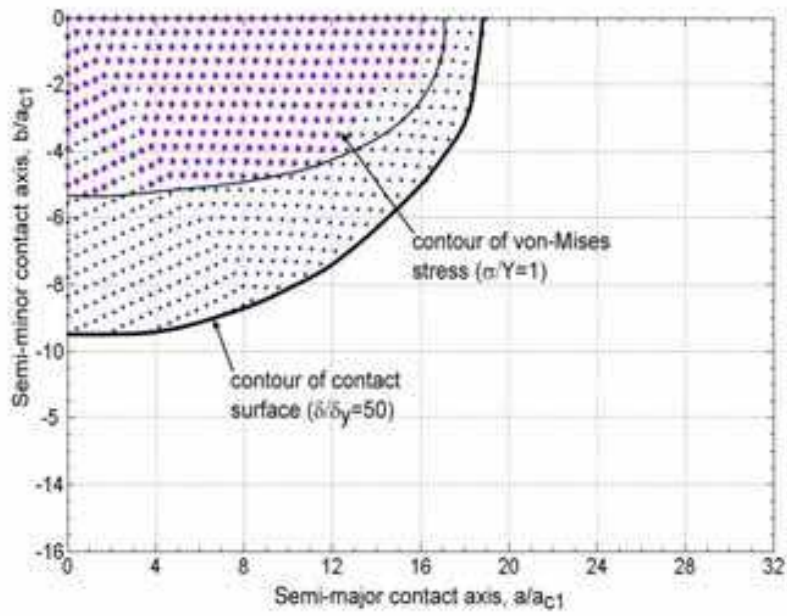
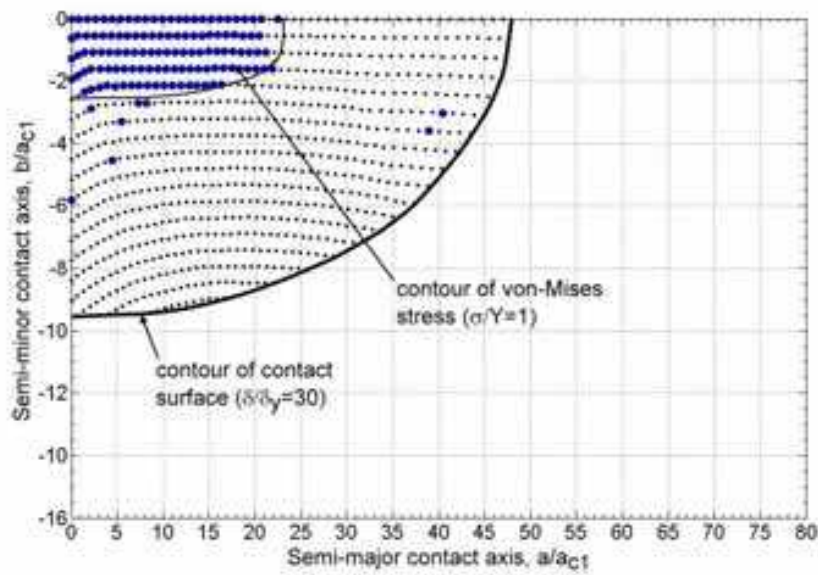
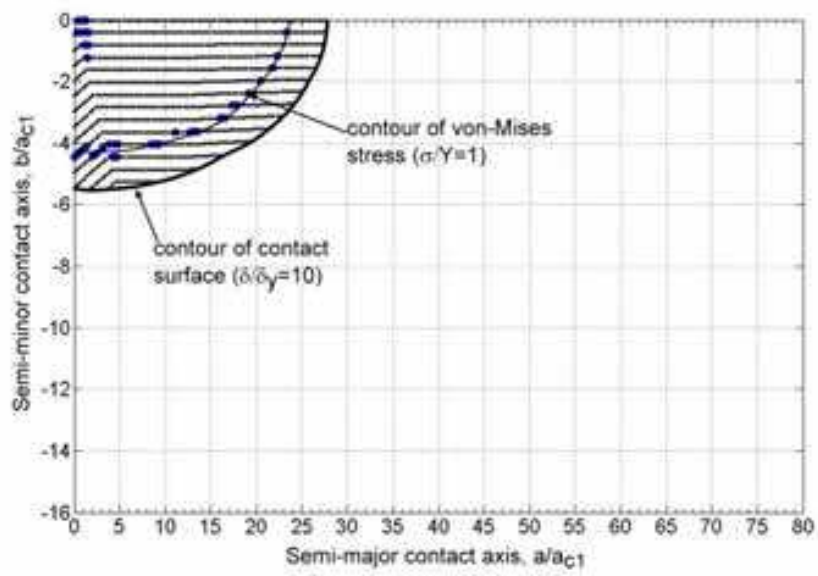


Fig. 9. Evolution of the plastic region on the contact surface of ellipsoid ( $k_e=1/2$ ) for  $10 \leq \delta / \delta_y \leq 90$



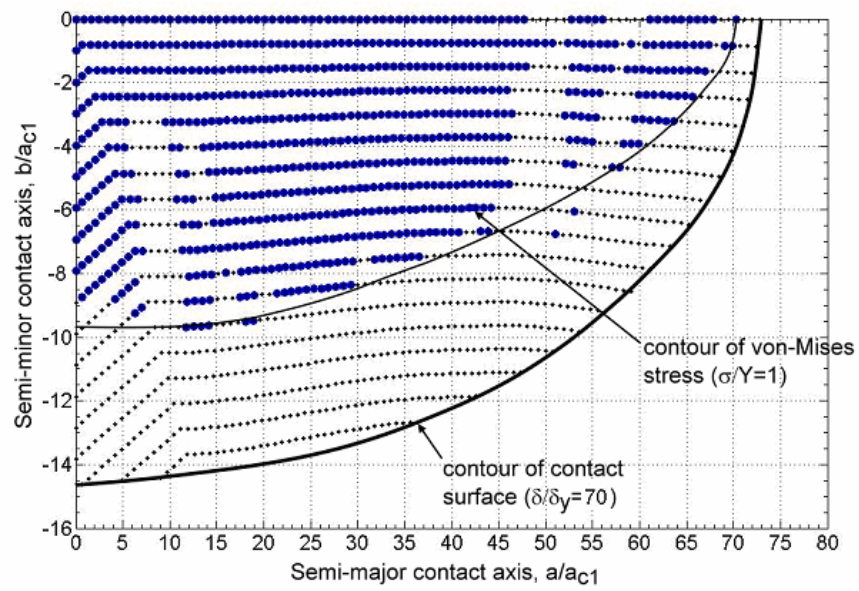
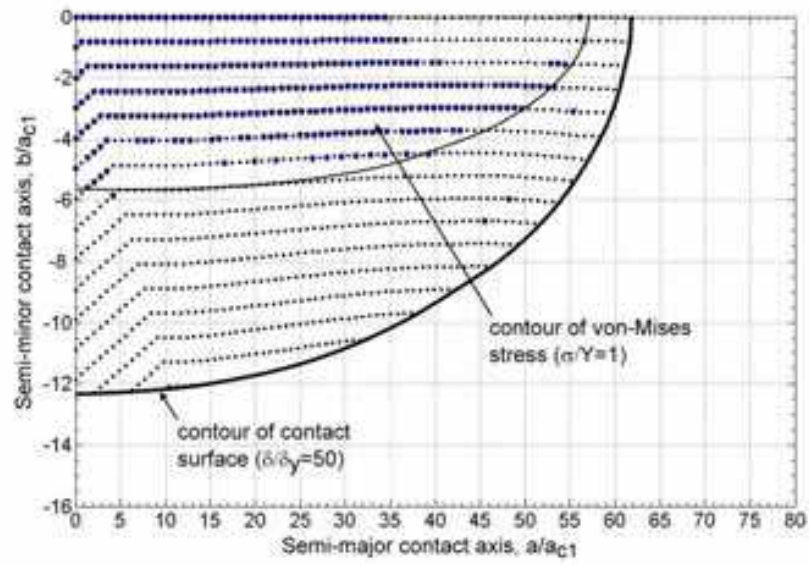


Fig. 10. Evolution of the plastic region on the contact surface of ellipsoid ( $k_e=1/5$ ) for  $10 \leq \delta / \delta_y \leq 70$ .

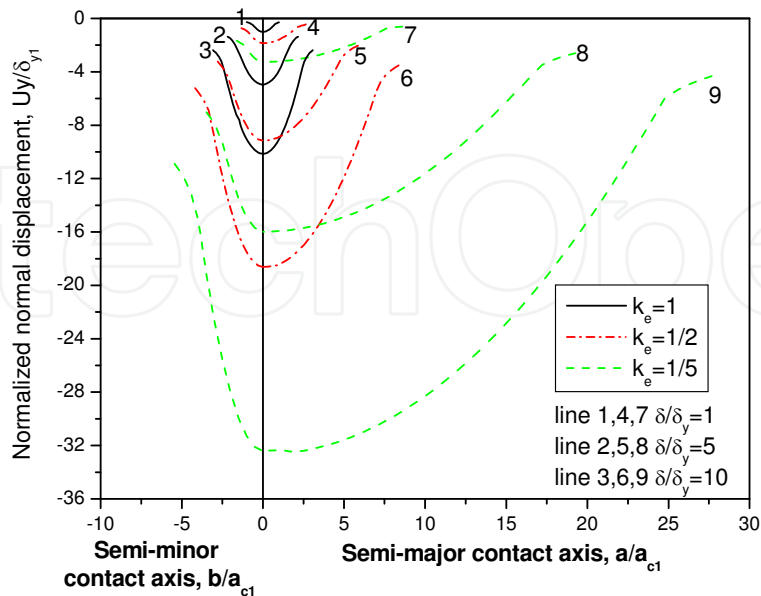


Fig. 11. The normalized normal displacement,  $U_y/\delta_{y1}$ , vs the Semi-major contact axis,  $a$ , and Semi-minor contact axis,  $b$ , for sphere ( $k_e=1$ ), ellipsoid ( $k_e=1/2$ ), ellipsoid ( $k_e=1/5$ ) in smaller interference depths.

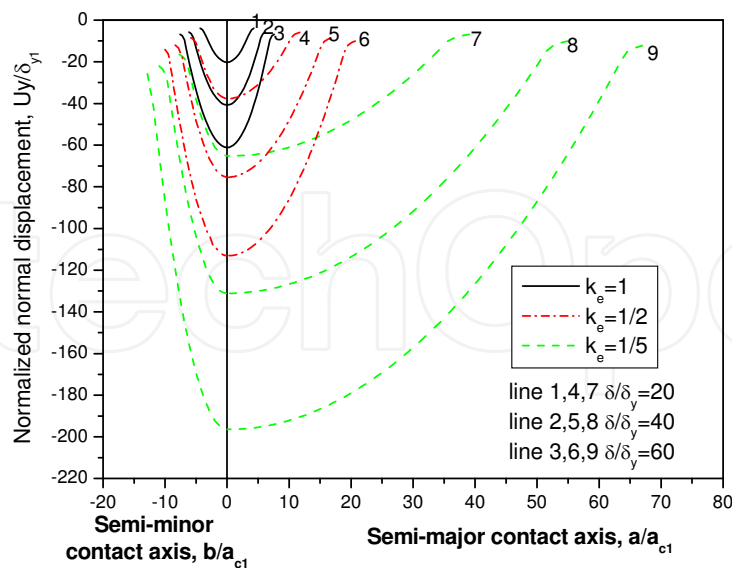


Fig. 12. The normalized normal displacement  $U_y/\delta_{y1}$  vs the Semi-major contact axis,  $a$ , and Semi-minor contact axis,  $b$ , for sphere ( $k_e=1$ ), ellipsoid ( $k_e=1/2$ ), ellipsoid ( $k_e=1/5$ ) in larger interference depths.

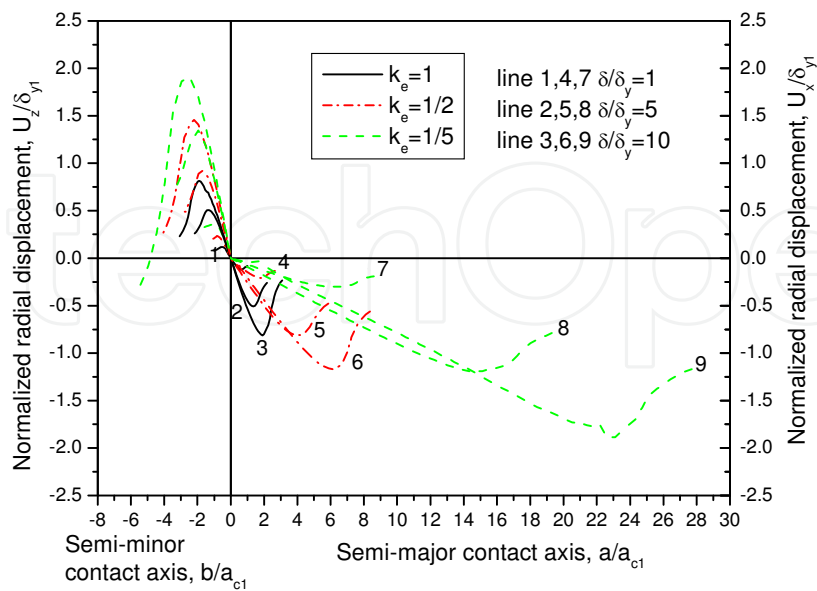


Fig. 13. The normalized radial displacement  $U_x/\delta_{y1}$  vs the Semi-major contact axis,  $a$ , and  $U_z/\delta_{y1}$  vs Semi-minor contact axis,  $b$ , for sphere ( $k_e=1$ ), ellipsoid ( $k_e=1/2$ ), ellipsoid ( $k_e=1/5$ ) in smaller interference depths.

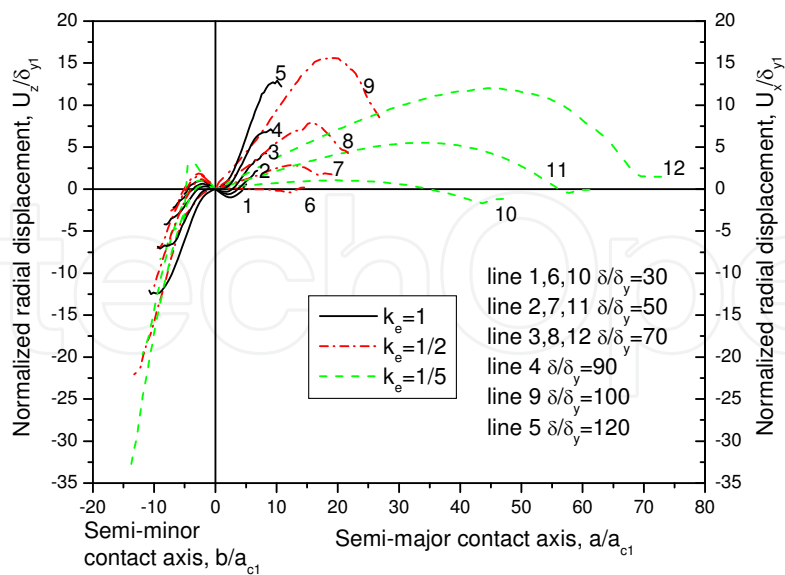


Fig. 14. The normalized radial displacement  $U_x/\delta_{y1}$  vs the Semi-major contact axis,  $a$ , and  $U_z/\delta_{y1}$  vs Semi-minor contact axis,  $b$ , for sphere ( $k_e=1$ ), ellipsoid ( $k_e=1/2$ ), ellipsoid ( $k_e=1/5$ ) in larger interference depths.

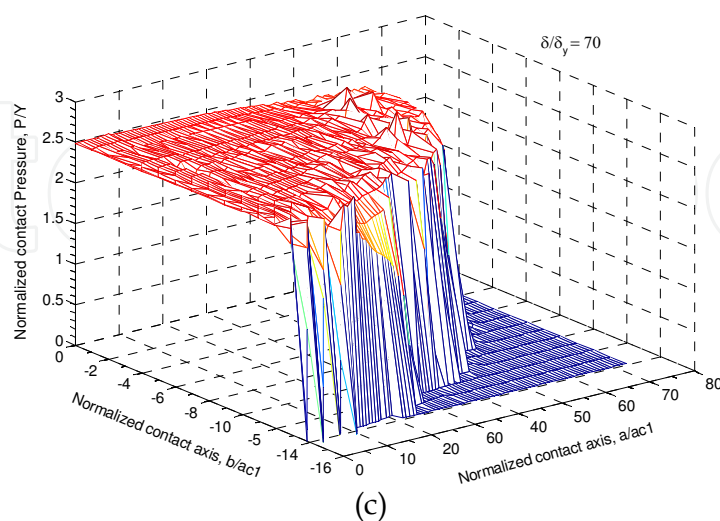
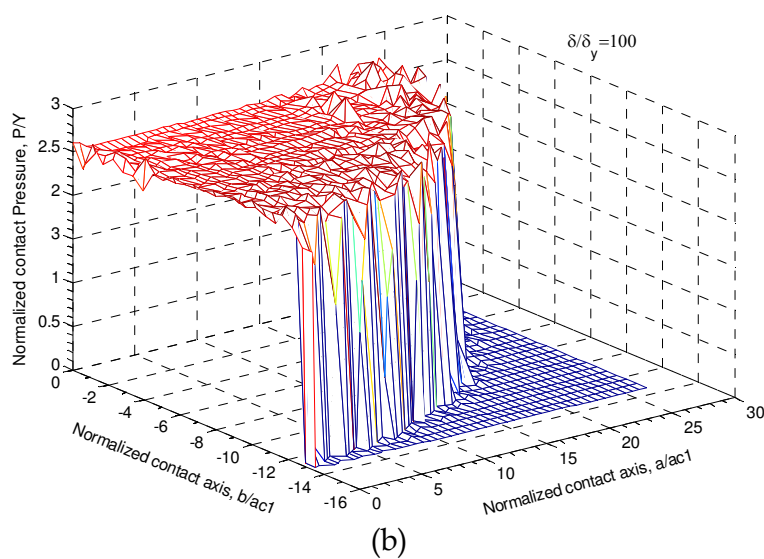
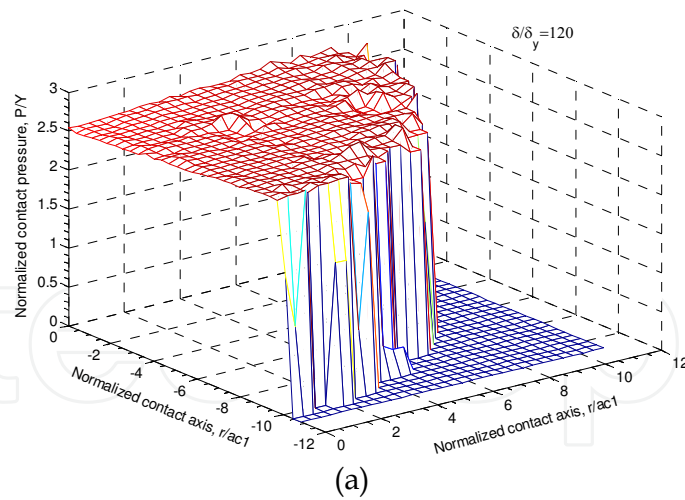


Fig. 15. The normalized contact pressure,  $P/Y$  vs Normalized contact axis,  $a/a_{c1}$ , and Semi-minor contact axis,  $b/a_{c1}$ , for (a) sphere ( $k_e=1$ ) at  $\delta/\delta_y=120$  (b) ellipsoid ( $k_e=1/2$ ) at  $\delta/\delta_y=100$ , (c) ellipsoid ( $k_e=1/5$ ) at  $\delta/\delta_y=70$ .

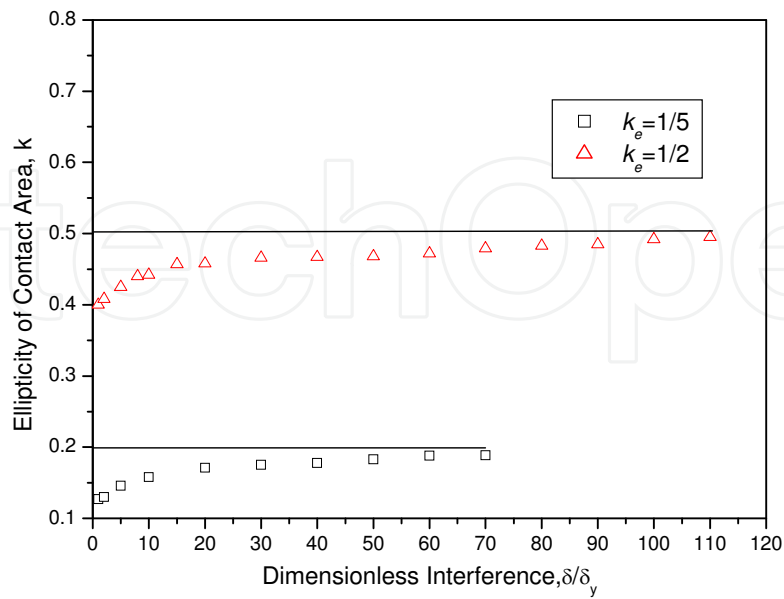


Fig. 16. Variations of the ellipticity of contact area with the dimensionless interference in the elastoplastic deformation regime.

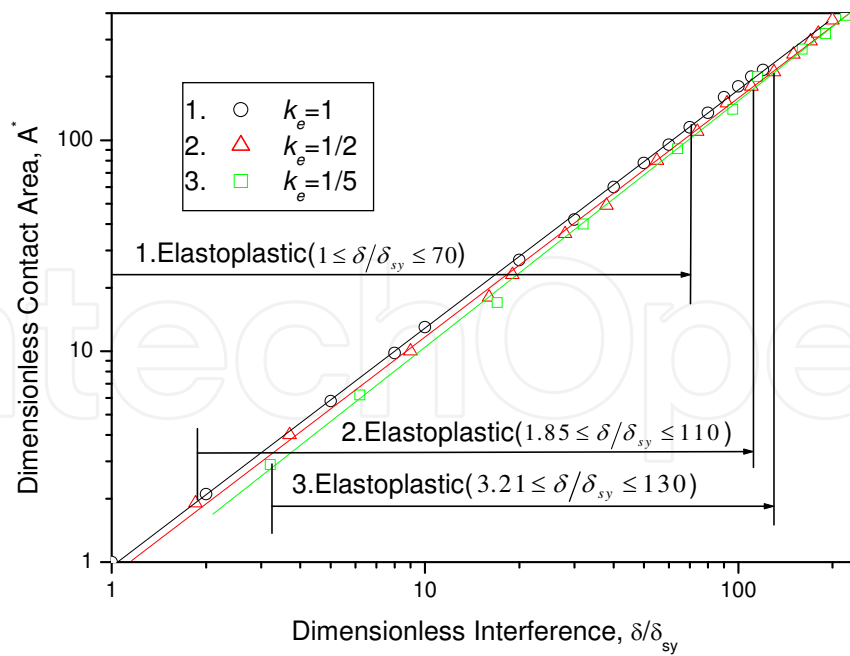


Fig. 17. Variations of the dimensionless contact area with the dimensionless interference.

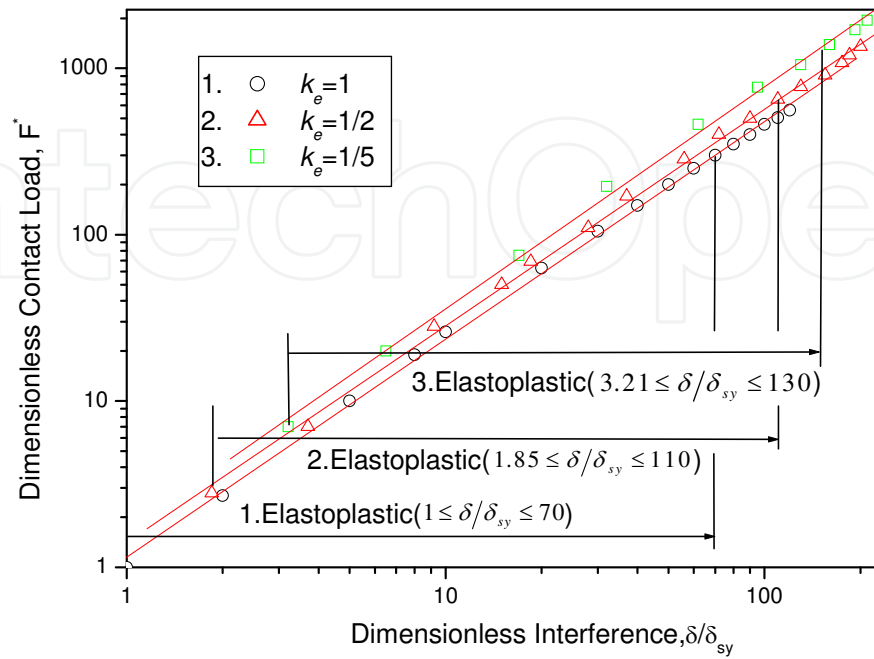


Fig. 18. Variations of the dimensionless contact load with the dimensionless interference.

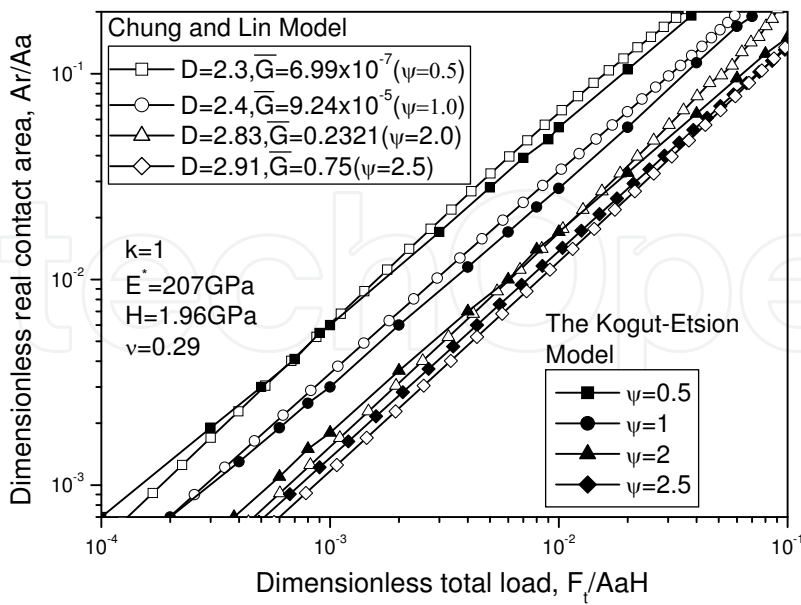


Fig. 19. Variations of the dimensionless real contact area with the dimensionless total load.

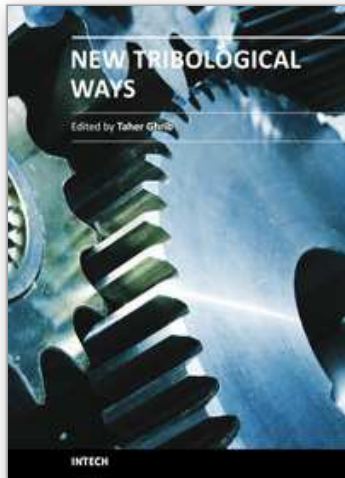
## 7. Reference

- Abbott, E. J. & Firestone, F. A. (1933). Specifying Surface Quality-A Method Based on Accurate Measurement and Comparison, *Mech. Eng. (Am. Soc. Mech. Eng.)*, 55, pp. 569-572.
- Belyaev N. M. (1957). Theory of Elasticity and Plasticity, *Moscow*.
- Bush, A. W.; Gibson, R. D. & Keogh, G. D. (1979). Strong Anisotropic Rough Surface, *ASME J Tribol.*, 101, pp. 15-20.
- Bryant M. D. & Keer L. M. (1982). Rough Contact Between Elastically and Geometrically Identical Curved Bodies, *ASME, J Appl. Mech.*, 49, pp. 345-352.
- Buczowski R. & Kleiber M. (2006). Elasto-plastic statistical model of strongly anisotropic rough surfaces for finite element 3D-contact analysis, *Comput. Methods Appl. Mech. Engrg.*, 195, pp. 5141-5161
- Chang, W. R.; Etsion, I. & Bogy, D. B. (1987). An Elastic-Plastic Model for the Contact of Rough Surfaces, *ASME J Tribol.*, 109, pp. 257-263.
- Chung, J. C. & Lin J. F. (2004). Fractal Model Developed for Elliptic Elastic-Plastic Asperity Microcontacts of Rough Surfaces, *ASME J Tribol.*, 126, pp. 82-88.
- Chung, J. C. (2010). Elastic-Plastic Contact Analysis of an Ellipsoid and a Rigid Flat, *Tribology International*, 43, pp. 491-502
- Greenwood, J. A. & Williamson, J. B. P. (1966). Contact of Nominally Flat Surfaces, *Proc. R. Soc. London, Ser. A*, 295, pp. 300-319.
- Greenwood, J. A. & Tripp, J. H. (1967). The Elastic Contact of Rough Spheres, *ASME J of Appl. Mech.*, Vol. 34, pp. 153-159.
- Greenwood, J. A. & Tripp, J. H. (1970-71). The Contact of Two Nominally Flat Rough Surfaces, *Proc. Instn. Mech. Engrs.*, Vol. 185, pp. 625-633
- Hisakado, T. (1974). Effects of Surface Roughness on Contact Between Solid Surfaces, *Wear*, Vol. 28, pp. 217-234.
- Hornig, J. H. (1998). An Elliptic Elastic-Plastic Asperity Microcontact Model for Rough Surface, *ASME J Tribol.*, 120, pp. 82-88.
- Johnson, K. L. (1985). Contact Mechanics, *Cambridge University Press*, Cambridge.
- Jeng, Y. R. & Wang P. Y. (2003). An Elliptical Microcontact Model considering Elastic, Elastoplastic, and Plastic Deformation, *ASME J Tribol.*, 125, pp. 232-240.
- Jackson, R. L. & Green I. (2005a). A Finite Element Study of Elasto-Plastic Hemispherical Contact Against a Rigid Flat, *ASME J Tribol.*, 127, pp. 343-354.
- Jackson, R. L.; Chusoipin I. & Green I. (2005b). A Finite Element Study of the Residual Stress and Deformation in Hemispherical Contacts, *ASME J Tribol.*, 127, pp. 484-493.
- Kogut, L. & Etsion, I. (2002). Elastic-Plastic Contact Analysis of a Sphere and a Rigid Flat, *ASME, J Appl. Mech.*, 69(5), pp. 657-662.
- Liu, G.; Wang, Q. J. & Lin, C. (1999). A Survey of Current Models for Simulating the Contact between Rough Surfaces, *Tribol. Trans.*, 42, pp. 581-591.
- Lin L. P., & Lin J. F. (2007). An Elliptical Elastic-Plastic Microcontact Model Developed for an Ellipsoid in Contact With a Smooth Rigid Flat, *ASME J Tribol.*, 129, pp. 772-782.
- Mindlin R. D. (1949). Compliance of Elastic Bodies in Contact, *ASME, J Appl. Mech.*, 7, pp. 259
- McCool, J. I. (1986). Comparison of Model for Contact of Rough Surfaces, *Wear*, Vol. 107, pp. 37-60.

- Pullen, J. & Williamson, J. B. P. (1972). On the Plastic Contact of Rough Surfaces, *Proc. Roy. Soc. (London)*, A 327, pp. 159-173.
- Zhao, Y.; Maletta, D. M., & Chang, L. (2000). An Asperity Microcontact Model Incorporating the Transition From Elastic Deformation to Fully Plastic Flow, *ASME J Tribol.*, 122, pp. 86-93.
- Sackfield, A. & Hills, D.A. (1983). Some Useful Results in the tangentially loaded Hertz Contact Problem, *J of Strain Analysis*, 18, pp. 107-110.

IntechOpen

IntechOpen



## **New Tribological Ways**

Edited by Dr. Taher Ghrib

ISBN 978-953-307-206-7

Hard cover, 498 pages

**Publisher** InTech

**Published online** 26, April, 2011

**Published in print edition** April, 2011

This book aims to recapitulate old information's available and brings new information's that are with the fashion research on an atomic and nanometric scale in various fields by introducing several mathematical models to measure some parameters characterizing metals like the hydrodynamic elasticity coefficient, hardness, lubricant viscosity, viscosity coefficient, tensile strength .... It uses new measurement techniques very developed and nondestructive. Its principal distinctions of the other books, that it brings practical manners to model and to optimize the cutting process using various parameters and different techniques, namely, using water of high-velocity stream, tool with different form and radius, the cutting temperature effect, that can be measured with sufficient accuracy not only at a research lab and also with a theoretical forecast. This book aspire to minimize and eliminate the losses resulting from surfaces friction and wear which leads to a greater machining efficiency and to a better execution, fewer breakdowns and a significant saving. A great part is devoted to lubrication, of which the goal is to find the famous techniques using solid and liquid lubricant films applied for giving super low friction coefficients and improving the lubricant properties on surfaces.

### **How to reference**

In order to correctly reference this scholarly work, feel free to copy and paste the following:

Jung Ching Chung (2011). The Elliptical Elastic-Plastic Microcontact Analysis, New Tribological Ways, Dr. Taher Ghrib (Ed.), ISBN: 978-953-307-206-7, InTech, Available from: <http://www.intechopen.com/books/new-tribological-ways/the-elliptical-elastic-plastic-microcontact-analysis>

**INTECH**  
open science | open minds

### **InTech Europe**

University Campus STeP Ri  
Slavka Krautzeka 83/A  
51000 Rijeka, Croatia  
Phone: +385 (51) 770 447  
Fax: +385 (51) 686 166  
[www.intechopen.com](http://www.intechopen.com)

### **InTech China**

Unit 405, Office Block, Hotel Equatorial Shanghai  
No.65, Yan An Road (West), Shanghai, 200040, China  
中国上海市延安西路65号上海国际贵都大饭店办公楼405单元  
Phone: +86-21-62489820  
Fax: +86-21-62489821

© 2011 The Author(s). Licensee IntechOpen. This chapter is distributed under the terms of the [Creative Commons Attribution-NonCommercial-ShareAlike-3.0 License](#), which permits use, distribution and reproduction for non-commercial purposes, provided the original is properly cited and derivative works building on this content are distributed under the same license.

IntechOpen

IntechOpen